# Genesis of the Sanhetun Tellurium-Gold Deposit, Northeast China: Constraints from In Situ Elemental and Sulfur Isotopic Compositions of Pyrite and U-pb Dating of Calcite

Mengmeng Zhang , Junfeng Shen , Chenglu Li * , M. Santosh , Kexin Xu , Gexue Zhao , Huajuan Gu , Jiajun Liu

Posted Date: 30 April 2024

doi: 10.20944/preprints202404.1971.v1

Keywords: telluride; pyrite; sulfur isotope; calcite; Sanhetun tellurium-gold deposit

 doi:10.20944/preprints202404.1971.v1



*Article*

# Genesis of the Sanhetun tellurium-Gold Deposit, Northeast China: Constraints from In Situ Elemental and Sulfur Isotopic Compositions of Pyrite and U-Pb Dating of Calcite

**Mengmeng Zhang [1,2], Junfeng Shen [1,2], Chenglu Li [3,*], M. Santosh [1,4,5], Kexin Xu [6], Gexue Zhao [7], Huajuan Gu [3] and Jiajun Liu [1]**

[1] School of Earth Sciences and Resources, China University of Geosciences, Beijing 100083, China; mmzhang0615@163.com (M.Z.); shenjf@cugb.edu.cn (J.S.); santosh@cugb.edu.cn (M.S.); liujiajun@cugb.edu.cn (J.L.)
[2] Research Center of Genetic Mineralogy, School of Earth Sciences and Resources, China University of Geosciences, Beijing 100083, China; mmzhang0615@163.com (M.Z.); shenjf@cugb.edu.cn (J.S.)
[3] Natural Resources Survey Institute of Heilongjiang Province, Harbin, 150036, China; 229010248@qq.com
[4] Department of Earth Science, University of Adelaide, Adelaide SA 5005, Australia; santosh@cugb.edu.cn
[5] Curtin Malaysia Research Institute, Curtin University, Malaysia, CDT 250, Miri, 98009, Sarawak, Malaysia; santosh@cugb.edu.cn
[6] School of Earth Sciences and Engineering, Nanjing University, Nanjing 210023, China; xukexin@nju.edu.cn
[7] School of Gemology, China University of Geosciences, Beijing 100083, China; Zhaogx@email.cugb.edu.cn
* Correspondence: lcl230881@163.com (C.L.)

**Abstract:** The Sanhetun tellurium-gold (Te-Au) deposit, located in the Duobaoshan polymetallic metallogenic belt (DPMB) within the eastern section of the Central Asian Orogenic Belt (CAOB), is a newly discovered small scale gold deposit. The mineralization, with resource of ≥ 4t Au, is mainly hosted in 3 NNE-trending alteration zones between granitic mylonite and volcanogenic-sedimentary formations. It's the genesis and timing of formation of this deposit are poorly constrained. Here, we report the results of petrographic studies, TESCAN Integrated Mineral Analyzer (TIMA), major and trace element concentrations, and in situ S isotope of pyrite and U-Pb ages of calcite. The results show that there are five species of telluride, including native tellurium, tetradymite, tsumoite, hessite and petzite and four types of pyrite, including coarse-grained euhedral Py1, fine-grained quartz-Py2 vein crosscutting Py1 and anhedral aggregated Py3 and Py4. The pre-ore Py1, containing negligible Au, Te and other trace elements, have a relatively narrow range of $\delta^{34}S$ values ranging from -1.20 to -0.57‰. The Py2 have slightly high concentrations of Au and Te and distinctly high concentrations of Mo, Sb, Zn and Mn with markedly positive $\delta^{34}S$ values of 4.67 to 14.43‰. The main ore stage Py3 contains high Au and Te concentrations and shows narrow $\delta^{34}S$ values ranging from -5.69 to 0.19‰. The post-ore stage Py4 contains low Au concentrations with the $\delta^{34}S$ values ranging from 2.66 to 3.86‰. Calcite from ore stage yield a U-Pb age of 135 ± 22 Ma, interpreted as the age of Te-Au mineralization. Our geochemical and geochronological data indicate that the Te was derived from partial melting of mantle metasomatized by the Te-rich fluids that originated from oceanic sediments. We correlate the tectonic setting with the subduction of Paleo Pacific plate in Early Cretaceous.

**Keywords:** telluride; pyrite; sulfur isotope; calcite; Sanhetun tellurium-gold deposit

## 1. Introduction

The Duobaoshan polymetallic metallogenic belt (DPMB) is an important Au-Cu-Mo-Fe ore field in NE China, with numerous ore deposits including the Zhengguang epithermal Au-Zn deposit, the Tongshan and Duobaoshan porphyry Cu-Mo deposits, and the Sankuanggou and Xiaoduobaoshan skarn Fe deposits[1–5]. In this belt, there is a large-scale NE-trending granitic mylonite ductile shear

 doi:10.20944/preprints202404.1971.v1



zone with maximum width of 25 km, within which a series of gold deposits were discovered, including the Sandaowanzi [6], Yongxin[7–9], Mengdehe [10] and Beidagou [11] deposits. Notably, these deposits show significant tellurium enrichment which is featured by the occurrence of telluride. The telluride commonly shows close relationship with Au mineralization, especially in the Sandaowanzi gold deposit which is a telluride-dominant epithermal gold deposit. Previous studies focused on the Au mineralization with not much attention paid to the Te enrichment mechanism and Te-Au relationship. In recent years, tellurium is listed as a critical metal [12] due to its potential application in the fields of photovoltaic cell, semiconductor materials and laser ladar[13–15], thus adding important significance to such type of deposits.

The Sanhetun Te-Au deposit is a newly discovered small scale gold deposit in the extreme southwestern part of the ductile shear zone. A number of tellurides were also recognized in this deposit [16]. However, the occurrence state, source of Te, Te-Au relationship and mineralizing age remain poorly understood. In this contribution, we present results from telluride mineralogy, in situ trace element compositions and sulfur isotope compositions of multiple types of pyrite and in situ U-Pb dating of calcite aiming at gaining insights into the genesis of Sanhetun Te-Au deposit.

## 2. Geological Settting

### *2.1. Reginal Geology*

The Duobaoshan polymetallic metallogenic belt (DPMB) is an important Cu-Au-Mo-Fe ore field in NE China and is located in the suture zone of the Xing'an and Songnen blocks within the eastern part of the Central Asian Orogenic Belt (CAOB) (Figure 1a). The Sanhetun Te-Au deposit occurs at the southwestern part of the DPMB (Figure 1b).

The regional strata are dominantly composed of the Neoarchean Xinkailing Formation, the Neoproterozoic to Lower Cambrian Galashan Formation, and the Beikuanhe Formation, primarily composed of schist, gneiss, amphibolite, and felsic volcanic rocks. The Ordovician strata from old to young are as followings: the Tongshan Formation consists of a sequence of sandstone interbedded with dolomite; the Duobaoshan Formation is composed of andesite, dacite, and volcanogenic-sedimentary rocks; the Luohe Formation and Aihui Formation consist of interlayered metamorphic sandstone, tuffaceous sandstone, and shale; the Silurian Huanghuagou Formation is a sequence of sandstone and siltstone. The Devonian Niqiuhe Formation consists of tuffaceous sandstone with interbeds of volcanic rocks. The Carboniferous-Permian Baoligaomiao Formation is mainly composed of intermediate-felsic volcanic rocks and volcaniclastic rocks. The Cretaceous strata consists of the Longjiang Formation, Guanghua Formation, Jiufengshan Formation, and Ganhe Formation, primarily composed of a suite of intermediate-mafic to intermediate-felsic volcanic rocks, volcaniclastic rocks, and volcanogenic-sedimentary rocks. The Cenozoic strata is mainly represented by the Daxiongshan basalt. The intrusive rocks include early to middle Ordovician diorite, granodiorite, and granodiorite porphyry, Early Carboniferous to Late Permian diorite granite, syenite, diorite, monzonite and alkali feldspar granite. Late Triassic to early to middle Jurassic magmatic rocks is composed of ultramafic rocks, gabbro, diorite granite, granodiorite, and quartz diorite. The Cretaceous magmatic rocks are mainly granite, granite porphyry, as well as vein rocks. The regional structure shows northeast and northwest trends, with secondary faults trending in east-west and north-south directions. The northwest-trending faults formed earlier, controlling the distribution of early Paleozoic strata and Cu (Mo), Au, and Ag deposits. The northeast-trending faults formed slightly later, controlling the distribution of regional late Paleozoic granites, Mesozoic volcanic rocks, and Au deposits [17].

 doi:10.20944/preprints202404.1971.v1



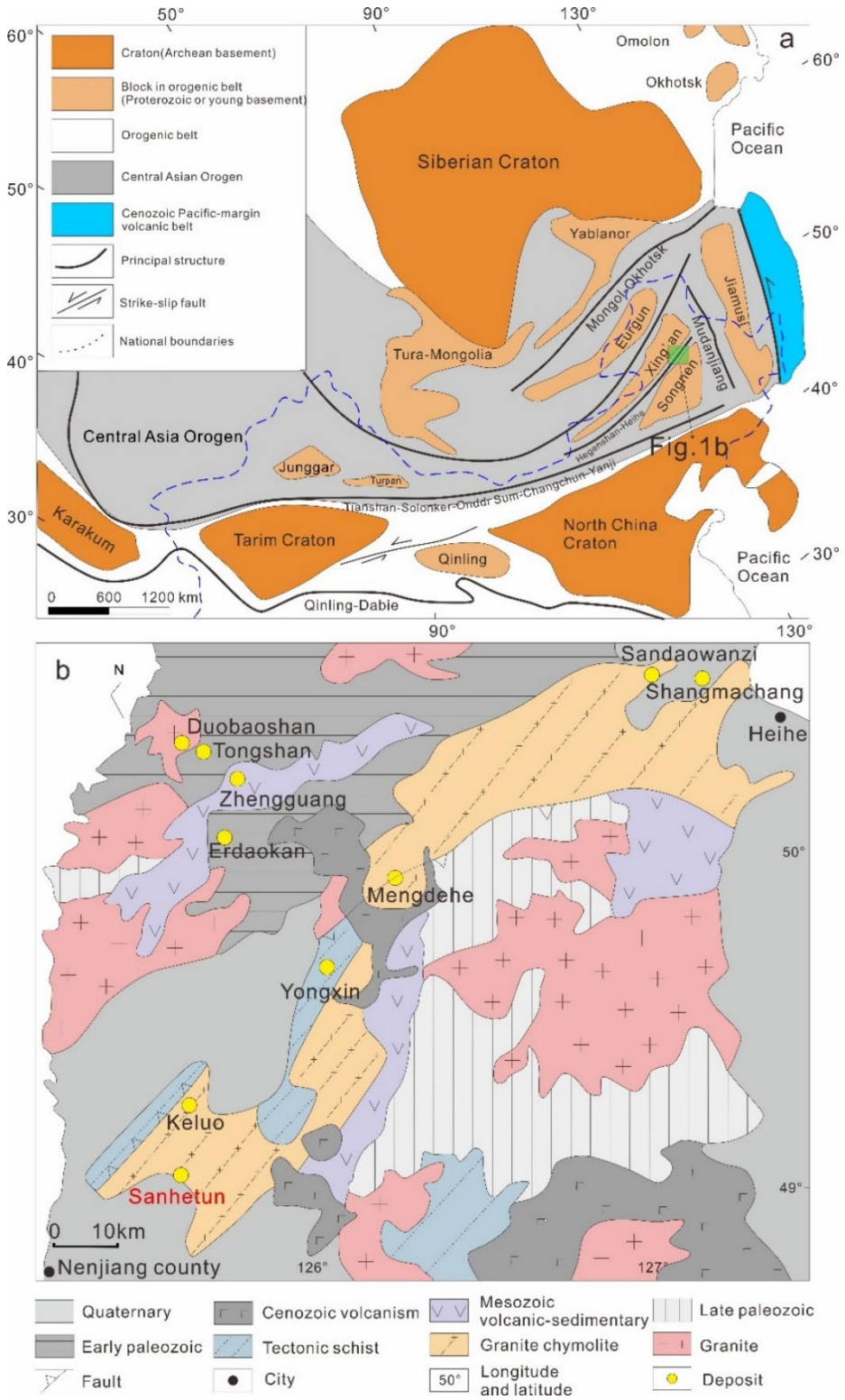


**Figure 1.** The geology of study area: (a) schematic tectonic map of the Central Asia Orogenic Belt (modified after [18]); (b) geological map of the Duobaoshan polymetallic metallogenic belt (modified after [19]).

*2.2. Deposit Geology*

The ore bodies are primarily located at the structural interfaces between the Lower Cretaceous Jiufengshan Formation and Ganhe Formation, which are composed of volcanogenic-sedimentary rock assemblages, and the Early Carboniferous granitic mylonite (Figure 2). The exposed strata in the

 doi:10.20944/preprints202404.1971.v1



mining area are mainly of Mesozoic volcanogenic-sedimentary rocks: the Guanghua Formation of the Lower Cretaceous is composed of intermediate to felsic volcanic sedimentary rocks, the Jiufengshan Formation consists of fine clastic sedimentary rocks interbedded with intermediate volcanic rocks, and the Ganhe Formation comprises intermediate-mafic volcanic rocks. The Upper Cretaceous Nenjiang Formation, consisting of mudstone and shale, unconformably overlies the aforementioned stratigraphic units. The intrusive rocks are mainly Early Carboniferous diorite granite and granodiorite, locally subjected to dynamic metamorphism forming mylonite and ultramylonite. Vein rocks mainly include diorite (porphyrite) veins and quartz veins.

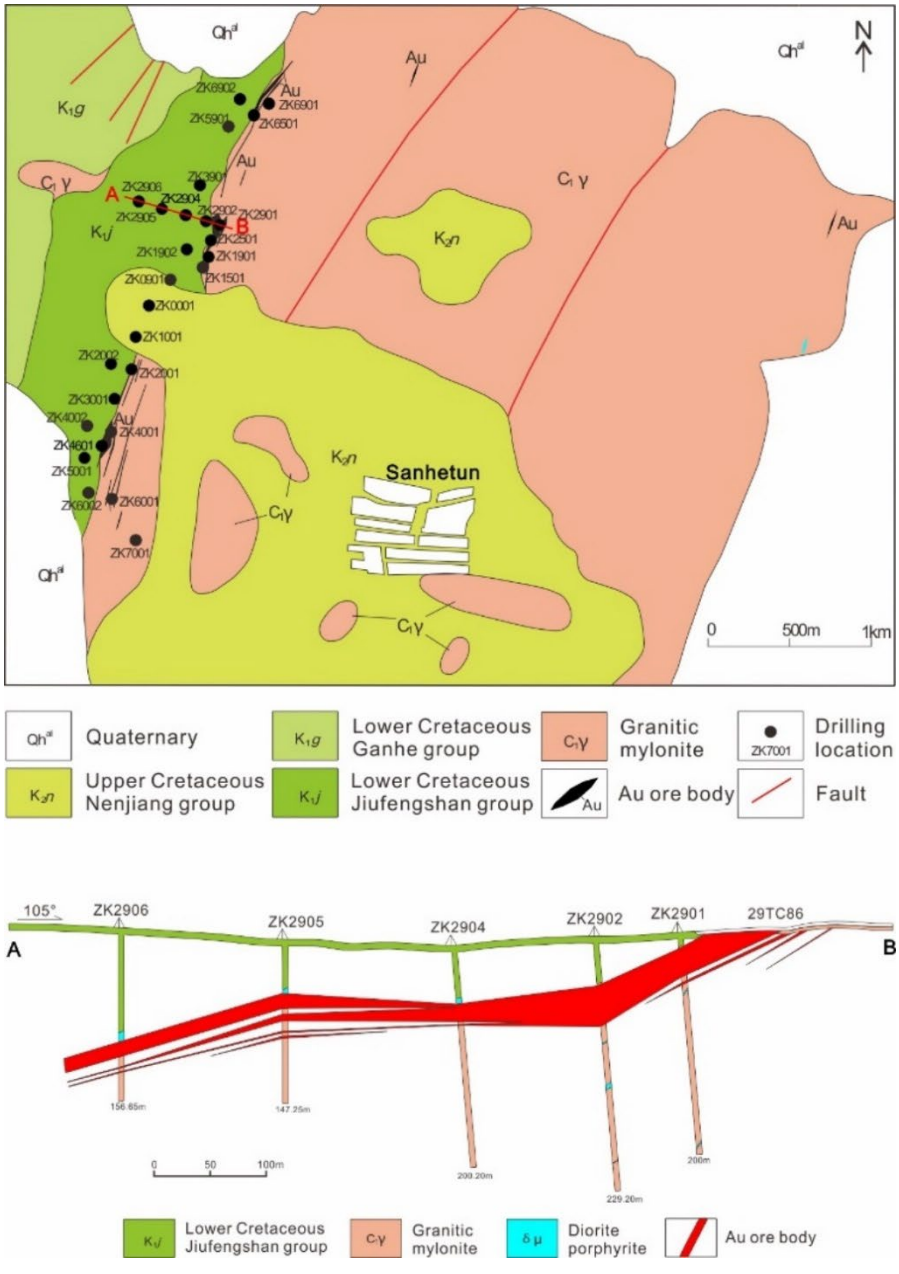


**Figure 2.** Geological map and cross-section of No. 29 exploration line of the Sanhetun Te-Au deposit (modified after [20]).

Up to now, three large-scale gold mineralized and pyritization altered zones have been delineated in the mining area, all showing NNE-trending linear parallel distribution, with some exhibiting lens-shaped distributions. The gold resource in the Sanhetun deposit is greater than 4 tons, with an average grade of 2.23 to 8.70 g/t [16]. The ores mainly consist of pyrite, which accounts for approximately 90% of the metallic minerals. Minor amounts of chalcopyrite, galena, sphalerite, and

 doi:10.20944/preprints202404.1971.v1



other minerals also occur. The main Au-bearing minerals consist of native gold and tellurides. The gangue minerals mainly consist of quartz, plagioclase, K-feldspar, biotite, sericite, chlorite, epidote, clay minerals, and minor amounts of carbonate minerals. The wall-rock alteration types mainly include silicification, sericitization, chloritization, and pyritization. Silicification and pyritization are closely related to gold mineralization (Figure 3).

Based on the mineral assemblage, structures, and crosscutting relationships, we identify five mineralization stages as follows. The pyrite-quartz stage (I), quartz-pyrite stage (II), gold-telluride-polymetallic sulfide stage (III), telluride-pyrite stage (IV), and carbonate stage (V). The stage (I) is characterized by milky quartz and minor disseminated pyrite (Py1) that displays euhedral to subhedral coarse-grained morphology (Figure 4d). The stage (II) is featured by fine-grained pyrite veinlets that crosscut Py1 (Figure 4e). The ore stage (III and IV) is characterized by anhedral aggregated pyrite (Py3 and Py4). Native gold, tetradymite, galena and chalcopyrite commonly coexist with Py3 (Figure 4f–h). Numerous tellurides mainly occur within the Py4 (Figure 4i). The main mineral assemblages of each stage are illustrated in Figure 5.

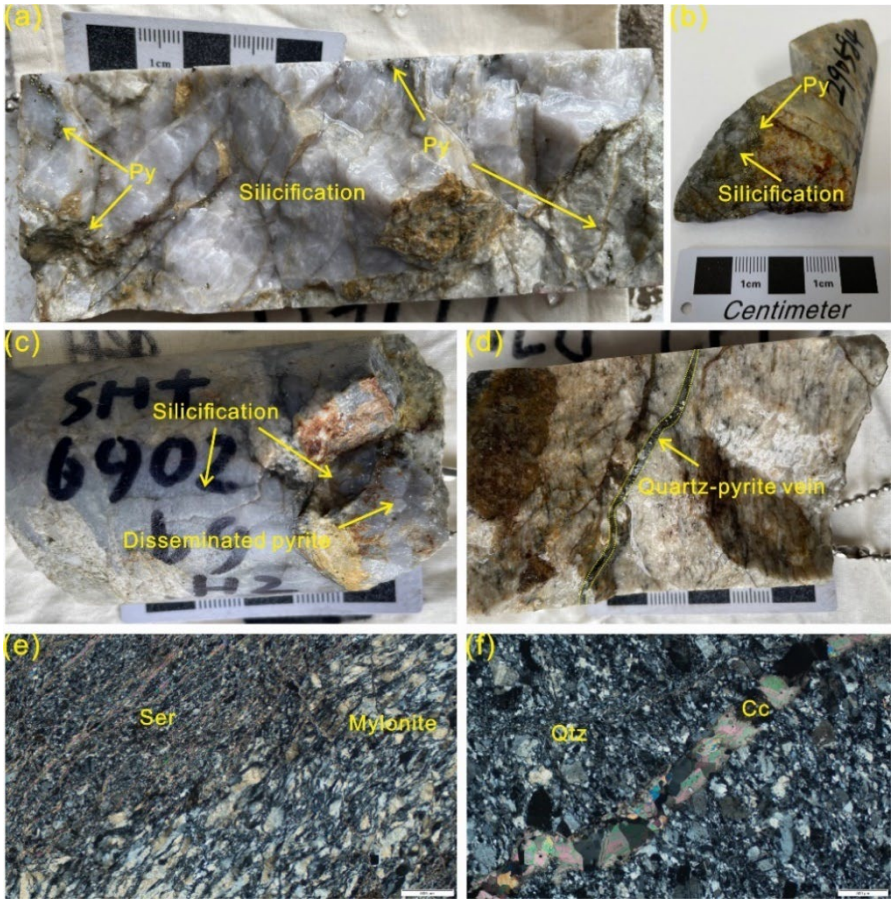


**Figure 3.** The main alteration types found within Sanhetun Te-Au deposit. (a-d) Strong silicification accompanied by pyritization; (e) sericitization mylonite; (f) carbonatization wall rocks. Cc—carbonite; Py—pyrite; Ser—sericite.

Preprints.org (www.preprints.org) | NOT PEER-REVIEWED | Posted: 30 April 2024 doi:10.20944/preprints202404.1971.v1



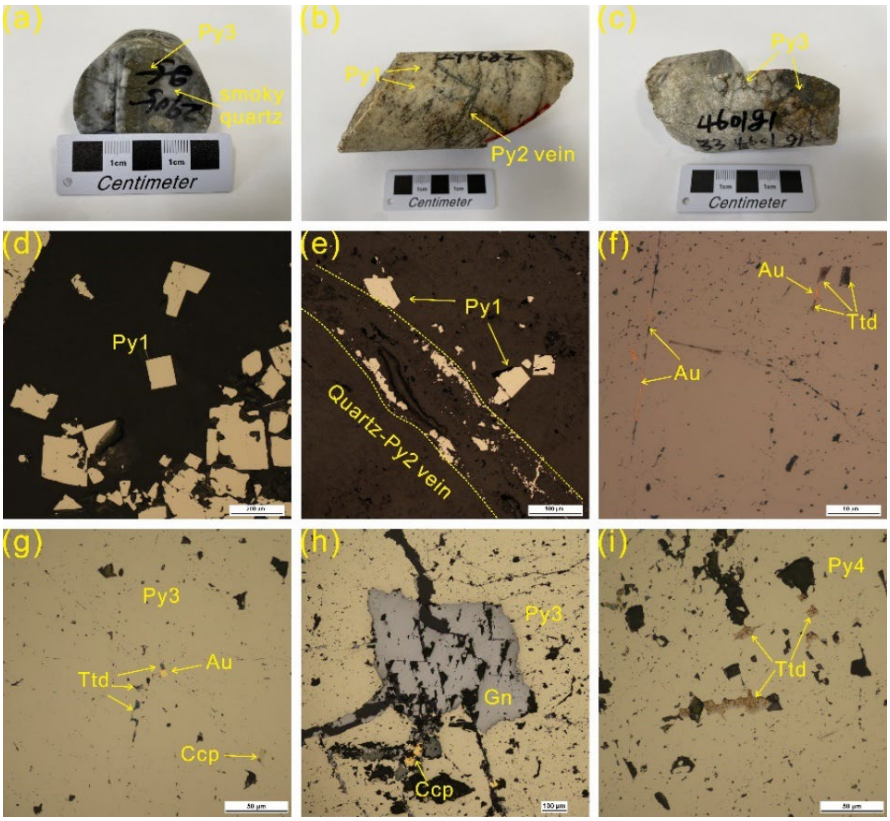


**Figure 4.** Ore features and photomicrographs of different mineralization stages from Sanhetun Te-Au deposit. (a-c) representative hand specimens of ore; (d) euhedral cubic Py1; (e) Py2 veinlets crosscut the euhedral Py1; (f, g) native gold coexist with tetradymite within Py3; (h) polymetallic sulfide in the main ore stage; (i) a number of tetradymite occur within the Py4. Au—native gold; Ccp—chalcopyrite; Py—pyrite; Gn—galena; Ttd—tetradymite.

| Stages / Minerals | Stage I | Stage II | Stage III | Stage IV | Stage V |
|---|---|---|---|---|---|
| Sericite | | | | | |
| Py1 | | | | | |
| Quartz | | | | | |
| Py2 | | | | | |
| Py3 | | | | | |
| Chalcopyrite | | | | | |
| Galena | | | | | |
| Native Au | | | | | |
| Tetradymite | | | | | |
| Py4 | | | | | |
| Hessite | | | | | |
| Petzite | | | | | |
| Tsumoite | | | | | |
| Native Te | | | | | |
| Calcite | | | | | |

 doi:10.20944/preprints202404.1971.v1



**Figure 5.** Paragenetic sequence of the major minerals in the Sanhetun Te-Au deposit. Note: The width of the lines represents relative abundance of minerals.

## 3. Materials and Methods

A total of more than 50 representative mineralized samples were collected from the drill cores of No. 29 cross section at different mining levels, which cover different mineralization stages in the Sanhetun Te-Au deposit. Polished thin sections were made from intensely pyritizatized ore samples to study petrographic characteristics, primary ore textures and identify unknown minerals under the reflected-transmitted light petrographic and scanning electron microscopy (SEM). Based on detailed microscopic observation, 20 polished thin sections were chosen to evaluate the species of tellurides and compositions of pyrite using the TESCAN Integrated Mineral Analyzer (TIMA), electron probe microanalysis (EPMA), laser ablation inductively coupled plasma mass spectrometry (LA-ICP-MS) and femtosecond laser ablation coupled multi-collector inductively coupled plasma mass spectrometry (fsLA-MC-ICP-MS) techniques.

### *3.1. TIMA Analyses*

TIMA (Tescan Integrated Mineral Analyzer) analyses were performed in the Institute of Geology, Chinese Academy of Geological Sciences (CAGS), Beijing. An automated mineralogy approach has been adopted for phase/mineral and element distribution mapping obtained by TIMA. The analyses were conducted on the thin section under dot-mapping mode with 25 kV accelerating voltage, 7.55 nA beam current, 15 mm working distance and 1 μm pixel size. The X-ray count of each point was 1000 kcps. Off-line processing software TIMA was used to identify minerals, and for data statistics and collation.

### *3.2. SEM Analyses*

SEM observations and energy-dispersive X-ray spectroscopy (EDS) point analyses were conducted on a TESCAN MIRA3-XMU scanning electron microscopy with an Oxford X-Max 20 EDS at the Research Center of Genetic Mineralogy, China University of Geosciences, Beijing. Operating conditions were a beam current of 75 nA, an accelerating voltage of 20 kV and working distance of 15 mm.

### *3.3. EPMA Analyses*

Major and trace element compositions of pyrite were analyzed using a JEOL JXA-8530F electron probe microanalyzer at the State Key Laboratory for Mineral Deposits Research, Nanjing university. Operating conditions were a beam current of 20 nA, an accelerating voltage of 15 kV and a 20 s counting time for all elements. The beam diameter was set at either 1 or 5 μm depending on the grain size being measured. Data were collected on a total of 12 elements, including 2 major elements Fe and S and 10 trace elements Au, Ag, As, Te, Se, Cu, Pb, Zn, Co and Ni. The standards used were native elements for Au, Ag and Te, pyrite for S and Fe, bismuth selenide for Bi and Se, pentlandite for Co and Ni, arsenopyrite for As, crocoite for Pb, sphalerite for Zn and chalcopyrite for Cu. ZAF corrections were made with proprietary JEOL software.

### *3.4. LA-ICP-MS Analyses*

Five representative polished thin sections were analyzed using the laser ablation-inductively coupled plasma-mass spectrometer at the Yanduzhongshi Geological Analysis Laboratories Ltd. Pyrite was analyzed using a Analytikjena M90 quadrupole ICPMS coupled with a 193 nm NWR193 Ar-F excimer laser for laser ablation. Ablation was performed within an atmosphere of ultra-high purity He at a flow rate of 0.9 L/min. The resulting aerosol was then mixed with Ar at a flow rate of 0.87 L/min immediately after exiting the ablation cell, through a T-connector, before entering the ICP [21]. For each analysis, a consistent spot diameter of 30 μm was used, with a frequency of 7 Hz and an energy of approximately 2 J/cm$^2$, for a duration of 40 seconds. Prior to each analysis, a gas blank

 doi:10.20944/preprints202404.1971.v1



measurement was conducted for 20 seconds. In the analysis process, external standards were employed to plot the calibration curve. Standard reference materials BCR-2G, NIST 612 and NIST 610, and were utilized for this purpose. To assess the accuracy of sulfide elements in the unknown samples, a sulfide standard MASS-1 was employed. To ensure the accuracy of the analyses, standard reference materials were measured after every 10-15 samples. In each spot analysis, detection limits of each element were calculated, allowing for the determination of the minimum concentration that can be reliably quantified. Data were collected on a total of 18 elements, including Au, Ag, As, Te, Bi, Se, Ge, Mo, Cd, Sb, Cu, Pb, Zn, Tl, Ti, Mn, Co, and Ni. The data processing was carried out using the ICPMSDataCal procedure.

### *3.5. In Situ Sulfur Isotope Analyses*

Pyrite in situ S isotope analyses were carried out using a RESOlution SE laser-ablation system attached to a Thermo Fisher Scientific Neptune Plus MC-ICP-MS at Createch Testing Tianjin Technology Co., Ltd. A spot size of 20-50 μm was employed with a 6-8 Hz repetition rate and an energy density of 6-8 J/cm2, depending on the S concentration of the samples. He (150 mL/min) was utilized as the carrier gas to efficiently purge aerosols from the ablation cell, and this gas was mixed with Ar (~0.8 L/min) in a T-connector before its entry into the ICP torch. The S isotopic data were acquired by static multi-collection in high-resolution mode. Prior to laser analyses, the Neptune MC-ICP-MS was tuned using a standard to obtain maximum sensitivity. Instrumental mass discrimination was calibrated using sample-standard bracketing method.

### *3.6. Calcite U-Pb Isotope Analyses*

The calcite U-Pb analyses were carried out in the Beijing ZKKY GeoAnalysis Laboratory Co., Ltd. using the Agilent 8900 ICP-MS, and a 193 nm NWR Excimer laser, with S155 dual volume sample cell. Laser conditions, including an energy of 6 mJ, a repetition rate of 10 Hz, and fluence of 5 J/cm$^2$ in a 120 μm diameter spots, were optimized to maximize signal strength and stability while ensuring that no melting occurred at the ablation site. The samples were analyzed with LA-ICP-MS in thin sections. Each static spot analysis consisted of 10 pre-ablation shots, 25 s of baseline data collection, 40 s sample ablation, and finally 20 s of washout.

## 4. Results

### *4.1. Telluride Mineralogy*

Because of the extremely fine grain size and scarce occurrence of tellurides, it is hard to locate the telluride accurately using the optical microscope and scanning electron microscope directly. TIMA is able to overcome this difficulty, which can identify all telluride grains within the scanned thin sections. All of the recognized telluride grains can be easily located and further verified by the EDS or EPMA. The results show that a number of tellurides occur in the Sanhetun Te-Au deposit including native tellurium, tetradymite, tsumoite, hessite and petzite (Figure 6). These tellurides commonly occur along the fracture or grain boundary of Py4 or as irregular patches within Py4 (Figure 4i). Among of them, tetradymite has closely spatial relationship with native gold within Py3 (Figure 4f,g). The detailed description of tellurides are as follows.

Tetradymite [$Bi_2Te_2S$] is the most abundant telluride in the Sanhetun Te-Au deposit, (Figure 6). Individual grains are commonly anhedral, ranging in size from 6 to 55 μm. Of note, tetradymite spatially associated with native gold (Figure 4f,g).

Hessite [$Ag_2Te$] is the next most abundant precious metal telluride and commonly coexist with petzite and galena. It is present usually as fine-grained and irregular patches enveloped within the pyrite (Figure 7c–e).

Petzite [$Ag_3AuTe_2$] is less abundant than the tetradymite and hessite, which has close relationship with native tellurium and hessite (Figure 7a,c–e).

 doi:10.20944/preprints202404.1971.v1



Native tellurium is rare in our sample set, which has intimate association with petzite. Individual grains are anhedral, ranging in size from 5 to 20 μm (Figure 7a).

Tsumoite [BiTe] is scarce and commonly occurs alone. Grain size is approximately 10 to 20 μm (Figure 7b).

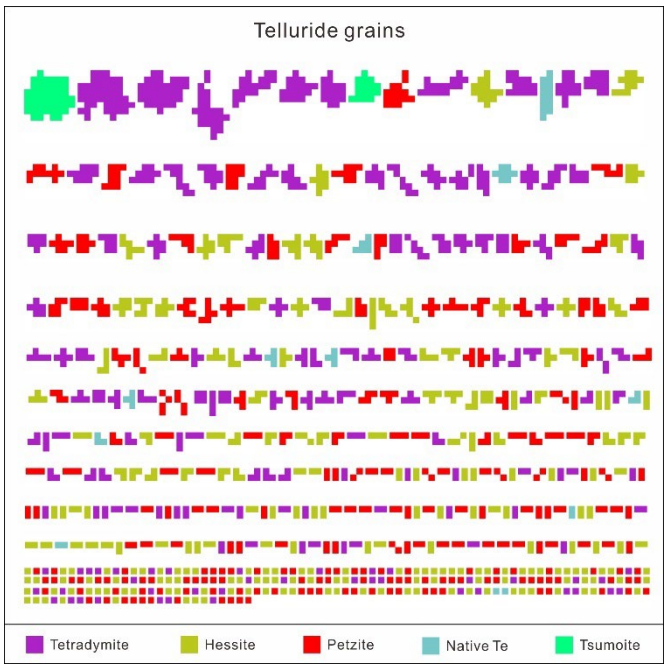


**Figure 6.** Independent tellurium-bearing mineral grains identified by TIMA in the Sanhetun Te-Au deposit.

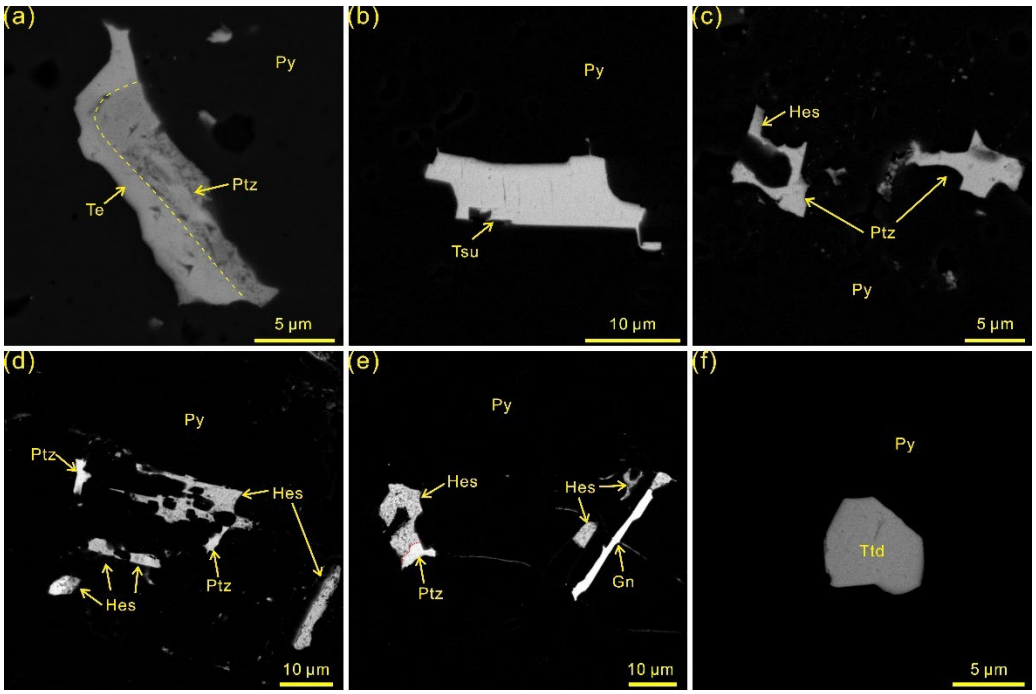


**Figure 7.** BSE images of tellurides from Sanhetun Te-Au deposit. (a) native Te coexists with petzite; (b) tsumoite occurs alone within pyrite; (c-e) hessite commonly coexists with petzite and galena; (f) tetradymite occurs alone within pyrite.

 doi:10.20944/preprints202404.1971.v1



*4.2. Pyrite Major and Trace Element Chemistry*

A total of 71 EPMA spot analyses were conducted on pyrite grains from different stages in the Sanhetun Te-Au deposit. The results are listed in Table 1. The data shows that all stages of pyrite have a similar S and Fe contents, from 52.54~53.98 wt.% and 46.03~47.31 wt.%, respectively. Gold and Ag are enriched in Py3 which has the highest concentrations of Au and Ag in comparison to Py1, Py2 and Py4, up to 0.13 and 0.17 wt.%. Arsenic concentrations are commonly low in all pyrite grains, less than 0.05 wt.%, indicating the As-poor pyrite from the Sanhetun deposit. Other minor components such as Cu, Pb, Zn, Co, Ni and Se are also detected by EPMA, but they show no significant variation in different pyrite stages.

**Table 1.** EPMA analyses of pyrite grains from the different stages in the Sanhetun Te-Au deposit (all values in wt. %).

| Stage | Sample no. | S | Fe | Au | Ag | Te | Se | As | Cu | Pb | Zn | Co | Ni | Total |
|---|---|---|---|---|---|---|---|---|---|---|---|---|---|---|
| | zk2904g7- | 52.6 | 46.0 | | 0.0 | 0.0 | | 0.0 | | 0.1 | 0.1 | 0.0 | 0.0 | 99.1 |
| Py1 | 1-1 | 42 | 26 | 0 | 11 | 43 | 0 | 06 | 0 | 97 | 33 | 88 | 1 | 56 |
| | zk2904g7- | 52.8 | 46.3 | | 0.0 | | | | | 0.0 | 0.0 | 0.0 | | 99.3 |
| Py1 | 1-2 | 69 | 47 | 0 | 13 | 0 | 0 | 0 | 0 | 67 | 41 | 4 | 0 | 77 |
| | zk2904g7- | 52.9 | 46.9 | | 0.0 | 0.0 | 0.0 | | 0.0 | | 0.0 | 0.0 | | 100. |
| Py1 | 1-3 | 67 | 98 | 0 | 09 | 03 | 23 | 0 | 17 | 0 | 13 | 53 | 0 | 08 |
| | zk2904g7- | 53.0 | 46.5 | | 0.0 | | 0.0 | 0.0 | 0.0 | 0.1 | 0.0 | 0.0 | 0.0 | 99.8 |
| Py1 | 1-4 | 1 | 79 | 0 | 28 | 0 | 12 | 26 | 05 | 32 | 03 | 41 | 01 | 37 |
| | zk2904g7- | 53.0 | 46.6 | | 0.0 | 0.0 | 0.0 | 0.0 | | 0.0 | 0.1 | 0.0 | | 99.8 |
| Py1 | 1-5 | 32 | 23 | 0 | 07 | 03 | 21 | 29 | 0 | 24 | 17 | 24 | 0 | 8 |
| | zk2904g7- | 53.0 | 46.7 | 0.0 | 0.0 | | | 0.0 | 0.0 | 0.0 | | 0.0 | | 99.9 |
| Py1 | 1-6 | 58 | 85 | 03 | 61 | 0 | 0 | 22 | 05 | 14 | 0 | 38 | 0 | 86 |
| | zk2904g7- | 53.1 | 47.0 | | | 0.0 | | | | 0.0 | | 0.0 | | 100. |
| Py1 | 1-7 | 46 | 22 | 0 | 0 | 05 | 0 | 0 | 0 | 73 | 0 | 59 | 0 | 31 |
| | zk2904g7- | 53.1 | 46.5 | | | | | | 0.0 | 0.0 | 0.0 | 0.0 | | 99.8 |
| Py1 | 1-8 | 71 | 68 | 0 | 0 | 0 | 0 | 0 | 19 | 1 | 8 | 36 | 0 | 84 |
| | zk2904g7- | 53.2 | 46.8 | | | | | | 0.0 | 0.0 | | 0.0 | | 100. |
| Py1 | 1-9 | 15 | 14 | 0 | 0 | 0 | 0 | 0 | 24 | 41 | 0 | 1 | 0 | 1 |
| | zk1001g2- | 53.2 | 46.7 | | 0.0 | | | | | 0.0 | 0.0 | | | 100. |
| Py1 | 1-1 | 45 | 07 | 0 | 04 | 0 | 0 | 0 | 0 | 13 | 39 | 0 | 0 | 01 |
| | zk1001g2- | 53.3 | 46.5 | | 0.0 | 0.0 | | 0.0 | 0.0 | | | 0.0 | | 100. |
| Py1 | 1-2 | 31 | 97 | 0 | 24 | 02 | 0 | 1 | 41 | 0 | 0 | 45 | 0 | 05 |
| | zk1001g2- | 53.3 | 46.5 | 0.0 | 0.0 | 0.0 | 0.0 | | 0.0 | | | 0.0 | | 100. |
| Py1 | 1-3 | 45 | 82 | 1 | 2 | 32 | 05 | 0 | 04 | 0 | 0 | 69 | 0 | 07 |
| | zk1001g2- | 53.3 | 46.8 | | 0.0 | | | | 0.0 | 0.0 | | 0.0 | 0.0 | 100. |
| Py1 | 1-4 | 5 | 93 | 0 | 39 | 0 | 0 | 0 | 32 | 32 | 0 | 62 | 02 | 41 |
| | zk1001g2- | 53.3 | 46.8 | 0.0 | 0.0 | 0.0 | | | 0.0 | | | 0.0 | | 100. |
| Py1 | 1-5 | 57 | 6 | 19 | 22 | 67 | 0 | 0 | 23 | 0 | 0 | 6 | 0 | 41 |
| | zk1001g2- | 53.3 | 46.4 | | 0.0 | | 0.0 | | | 0.0 | 0.0 | 0.0 | | |
| Py1 | 1-6 | 92 | 81 | 0 | 22 | 0 | 17 | 0 | 0 | 65 | 22 | 05 | 0 | 100 |

 doi:10.20944/preprints202404.1971.v1



| | | | | | | | | | | | | | | |
|---|---|---|---|---|---|---|---|---|---|---|---|---|---|---|
| | zk1001g2- | 53.4 | 46.1 | | | 0.0 | | | | | 0.0 | 0.0 | | 99.7 |
| Py1 | 1-7 | 09 | 86 | 0 | 0 | 99 | 0 | 0 | 0 | 0 | 48 | 53 | 0 | 95 |
| | zk1001g2- | 53.4 | 47.1 | | | 0.0 | 0.0 | | 0.0 | 0.0 | 0.0 | 0.0 | | 100. |
| Py1 | 1-8 | 19 | 38 | 0 | 0 | 1 | 61 | 0 | 17 | 7 | 39 | 21 | 0 | 78 |
| | zk1001g2- | 53.4 | 46.8 | | 0.0 | | 0.0 | 0.0 | 0.0 | 0.0 | 0.0 | 0.0 | | 100. |
| Py1 | 1-9 | 32 | 19 | 0 | 41 | 0 | 19 | 29 | 04 | 13 | 09 | 29 | 0 | 4 |
| | zk1001g2- | 53.4 | 46.3 | | | 0.0 | 0.0 | 0.0 | | 0.0 | | 0.0 | 0.0 | 100. |
| Py1 | 1-10 | 46 | 46 | 0 | 0 | 58 | 75 | 23 | 0 | 3 | 0 | 26 | 13 | 02 |
| | zk2905g5- | 53.4 | 46.3 | | | | | | | | 0.0 | 0.0 | | 99.8 |
| Py2 | 1-1 | 55 | 3 | 0 | 0 | 0 | 0 | 0 | 0 | 0 | 84 | 24 | 0 | 93 |
| | zk2905g5- | 53.4 | 46.5 | | | | | 0.0 | 0.0 | | 0.0 | 0.0 | 0.0 | 100. |
| Py2 | 1-2 | 68 | 77 | 0 | 0 | 0 | 0 | 04 | 64 | 0 | 34 | 24 | 83 | 25 |
| | zk2905g5- | 53.4 | 46.9 | 0.0 | | | | | 0.0 | 0.0 | | 0.0 | 0.0 | 100. |
| Py2 | 1-3 | 76 | 96 | 13 | 0 | 0 | 0 | 0 | 37 | 84 | 0 | 45 | 31 | 68 |
| | zk2905g5- | 53.4 | 46.6 | | 0.0 | 0.0 | | | | 0.0 | 0.0 | 0.0 | | 100. |
| Py2 | 1-4 | 84 | 82 | 0 | 15 | 17 | 0 | 0 | 0 | 05 | 19 | 53 | 0 | 28 |
| | zk2905g5- | 53.4 | 47.0 | 0.0 | 0.0 | | | | 0.0 | 0.0 | | 0.0 | | 100. |
| Py2 | 1-5 | 84 | 57 | 03 | 65 | 0 | 0 | 0 | 21 | 24 | 0 | 43 | 0 | 7 |
| | zk2905g5- | 53.4 | 46.6 | | 0.0 | | | | | 0.0 | | 0.0 | | 100. |
| Py2 | 1-6 | 92 | 26 | 0 | 04 | 0 | 0 | 0 | 0 | 64 | 0 | 1 | 0 | 2 |
| | zk2905g5- | 53.5 | 46.5 | | | 0.0 | 0.0 | | 0.0 | | 0.0 | | | 100. |
| Py2 | 1-7 | 1 | 29 | 0 | 0 | 47 | 04 | 0 | 02 | 0 | 26 | 0 | 0 | 12 |
| | zk2905g5- | 53.5 | 46.8 | | | | 0.0 | | | 0.1 | 0.0 | 0.0 | | 100. |
| Py2 | 1-8 | 64 | 48 | 0 | 0 | 0 | 5 | 0 | 0 | 38 | 58 | 52 | 0 | 71 |
| | zk2905g5- | 53.5 | 46.8 | | 0.0 | | | | 0.0 | 0.0 | | 0.0 | | 100. |
| Py2 | 1-9 | 93 | 12 | 0 | 02 | 0 | 0 | 0 | 33 | 37 | 0 | 14 | 0 | 49 |
| | zk2905g5- | 53.5 | 46.7 | | 0.0 | 0.0 | | | | | 0.0 | 0.0 | | 100. |
| Py2 | 1-10 | 96 | 29 | 0 | 02 | 35 | 0 | 0 | 0 | 0 | 37 | 1 | 0 | 41 |
| | zk2905g5- | 53.6 | 46.7 | | | | 0.0 | 0.0 | 0.0 | 0.0 | | 0.0 | | 100. |
| Py2 | 1-11 | 47 | 42 | 0 | 0 | 0 | 04 | 19 | 26 | 35 | 0 | 4 | 0 | 51 |
| | zk2905g5- | 53.6 | 46.7 | 0.0 | | | | | | 0.0 | | | 0.0 | 100. |
| Py2 | 1-12 | 51 | 56 | 19 | 0 | 0 | 0 | 0 | 0 | 19 | 0 | 0 | 36 | 48 |
| | zk2905g5- | 53.6 | 46.9 | 0.0 | | 0.0 | | | 0.0 | 0.0 | 0.0 | 0.0 | | 100. |
| Py2 | 1-13 | 67 | 16 | 16 | 0 | 15 | 0 | 0 | 41 | 13 | 29 | 28 | 0 | 73 |
| | zk2905g5- | 53.6 | 47.0 | | 0.0 | | | 0.0 | | 0.0 | | 0.0 | | 100. |
| Py2 | 1-14 | 85 | 27 | 0 | 13 | 0 | 0 | 35 | 0 | 27 | 0 | 83 | 0 | 87 |
| | zk2905g5- | | 47.1 | | | | | 0.0 | 0.0 | | | 0.0 | | 100. |
| Py2 | 1-15 | 53.7 | 38 | 0 | 0 | 0 | 0 | 03 | 38 | 0 | 0 | 21 | 0 | 9 |
| | zk2905g5- | 53.7 | 46.6 | 0.0 | | 0.0 | 0.0 | | | 0.0 | | 0.0 | | 100. |
| Py2 | 1-16 | 06 | 83 | 03 | 0 | 84 | 32 | 0 | 0 | 56 | 0 | 31 | 0 | 6 |
| | zk2905g5- | 53.7 | 46.4 | | | | 0.0 | 0.0 | | 0.0 | 0.0 | 0.0 | 0.0 | 100. |
| Py2 | 1-17 | 1 | 08 | 0 | 0 | 0 | 5 | 04 | 0 | 21 | 61 | 45 | 08 | 31 |

 doi:10.20944/preprints202404.1971.v1



| | | | | | | | | | | | | | | |
|---|---|---|---|---|---|---|---|---|---|---|---|---|---|---|
| | zk2905g5- | 53.7 | 46.9 | | 0.0 | 0.0 | | | 0.0 | 0.0 | | | 0.0 | 100. |
| Py2 | 1-18 | 24 | 85 | 0 | 33 | 18 | 0 | 0 | 13 | 72 | 0 | 0 | 12 | 86 |
| | zk2905g5- | 53.7 | 46.9 | | 0.0 | | | | | 0.0 | 0.0 | | | 100. |
| Py2 | 1-19 | 42 | 05 | 0 | 24 | 0 | 0 | 0 | 0 | 32 | 42 | 0 | 0 | 75 |
| | zk2905g5- | 53.7 | 46.9 | | | 0.0 | | | | 0.0 | 0.0 | | | 100. |
| Py2 | 1-20 | 6 | 52 | 0 | 0 | 28 | 0 | 0 | 0 | 86 | 09 | 0 | 0 | 84 |
| | zk2905g5- | 53.8 | 47.0 | | | | | 0.0 | 0.0 | 0.0 | | 0.0 | 0.0 | 100. |
| Py2 | 1-21 | 14 | 11 | 0 | 0 | 0 | 0 | 13 | 21 | 67 | 0 | 55 | 1 | 99 |
| | zk2905g5- | 53.8 | 46.2 | | | | | 0.0 | 0.0 | 0.0 | 0.0 | | | 100. |
| Py2 | 1-22 | 2 | 93 | 0 | 0 | 0 | 0 | 3 | 43 | 11 | 32 | 0 | 0 | 23 |
| | zk2905g5- | 53.9 | 46.5 | | 0.0 | 0.0 | | 0.0 | 0.0 | | 0.0 | 0.0 | | 100. |
| Py2 | 1-23 | 14 | 43 | 0 | 24 | 12 | 0 | 12 | 76 | 0 | 15 | 64 | 0 | 66 |
| | zk2905g5- | 53.9 | 46.5 | | | | | | | 0.0 | | | | 100. |
| Py2 | 1-24 | 33 | 79 | 0 | 0 | 0 | 0 | 0 | 0 | 35 | 0 | 0 | 0 | 55 |
| | zk2905g3- | 53.9 | 46.5 | | 0.0 | | | | | | 0.0 | 0.1 | | 100. |
| Py3 | 1 | 47 | 19 | 0 | 37 | 0 | 0 | 0 | 0 | 0 | 76 | 05 | 0 | 68 |
| | zk2905g3- | 53.9 | 46.6 | 0.0 | 0.0 | 0.0 | | | | 0.0 | 0.0 | 0.0 | | 100. |
| Py3 | 2 | 82 | 44 | 16 | 22 | 33 | 0 | 0 | 0 | 64 | 06 | 26 | 0 | 79 |
| | zk2905g3- | 52.5 | 46.3 | 0.0 | 0.0 | | | | | | 0.0 | 0.0 | 0.0 | 99.1 |
| Py3 | 3 | 43 | 66 | 22 | 74 | 0 | 0 | 0 | 0 | 0 | 39 | 83 | 13 | 4 |
| | zk2905g3- | 52.5 | 46.5 | 0.0 | | | | | | 0.0 | 0.0 | 0.0 | 0.0 | 99.2 |
| Py3 | 4 | 51 | 47 | 8 | 0 | 0 | 0 | 0 | 0 | 38 | 34 | 35 | 07 | 92 |
| | zk2905g3- | 53.8 | 46.6 | 0.0 | | 0.0 | | 0.0 | 0.0 | 0.0 | 0.0 | 0.1 | 0.0 | 100. |
| Py3 | 5 | 73 | 49 | 22 | 0 | 07 | 0 | 17 | 11 | 68 | 25 | 52 | 06 | 83 |
| | zk2905g3- | 53.8 | 46.8 | 0.0 | 0.0 | | 0.0 | 0.0 | | 0.0 | 0.0 | 0.0 | 0.0 | 100. |
| Py3 | 6 | 79 | 42 | 22 | 07 | 0 | 46 | 03 | 0 | 48 | 43 | 59 | 1 | 96 |
| | zk2905g3- | 53.2 | 47.3 | 0.0 | | | | | | | 0.0 | 0.0 | | 100. |
| Py3 | 7 | 35 | 05 | 42 | 0 | 0 | 0 | 0 | 0 | 0 | 19 | 52 | 0 | 65 |
| | zk2905g3- | 53.2 | 46.5 | 0.0 | 0.0 | 0.0 | 0.0 | 0.0 | | | 0.0 | 0.0 | | 100. |
| Py3 | 8 | 53 | 7 | 35 | 26 | 28 | 18 | 17 | 0 | 0 | 54 | 24 | 0 | 03 |
| | zk2905g3- | 53.3 | 46.8 | 0.0 | | | 0.0 | 0.0 | | | | 0.0 | 0.0 | 100. |
| Py3 | 9 | 35 | 53 | 29 | 0 | 0 | 08 | 06 | 0 | 0 | 0 | 34 | 65 | 33 |
| | zk2905g3- | 53.3 | 46.4 | 0.0 | | | 0.0 | 0.0 | | | 0.0 | 0.0 | | 99.9 |
| Py3 | 10 | 74 | 64 | 22 | 0 | 0 | 14 | 04 | 0 | 0 | 19 | 14 | 0 | 11 |
| | zk2905g3- | 53.4 | 46.4 | 0.0 | | 0.0 | 0.0 | 0.0 | 0.0 | | 0.0 | 0.0 | | 100. |
| Py3 | 11 | 02 | 26 | 29 | 0 | 48 | 26 | 44 | 21 | 0 | 27 | 16 | 0 | 04 |
| | zk2905g3- | 53.4 | 46.6 | 0.0 | | 0.0 | 0.0 | | | 0.1 | | 0.0 | 0.0 | 100. |
| Py3 | 12 | 2 | 57 | 26 | 0 | 77 | 26 | 0 | 0 | 02 | 0 | 45 | 57 | 41 |
| | zk2905g3- | 53.4 | 46.6 | 0.0 | | | 0.0 | 0.0 | | 0.0 | | 0.0 | | 100. |
| Py3 | 13 | 65 | 24 | 41 | 0 | 0 | 15 | 01 | 0 | 02 | 0 | 1 | 0 | 16 |
| | zk2905g3- | 53.5 | 46.8 | 0.0 | | 0.0 | 0.0 | | 0.0 | 0.0 | 0.0 | 0.0 | 0.0 | 100. |
| Py3 | 14 | 3 | 81 | 35 | 0 | 22 | 06 | 0 | 31 | 29 | 11 | 38 | 13 | 6 |

 doi:10.20944/preprints202404.1971.v1



| | | | | | | | | | | | | | | |
|---|---|---|---|---|---|---|---|---|---|---|---|---|---|---|
| | zk2905g5- | 53.5 | 47.0 | 0.0 | 0.0 | | 0.0 | | 0.0 | 0.0 | | | | 100. |
| Py4 | 2-1 | 93 | 49 | 26 | 41 | 0 | 12 | 0 | 3 | 6 | 0 | 0 | 0 | 81 |
| | zk2905g5- | 53.6 | 46.7 | 0.0 | 0.0 | | | 0.0 | 0.0 | 0.0 | | 0.0 | 0.0 | 100. |
| Py4 | 2-2 | 67 | 6 | 54 | 63 | 0 | 0 | 2 | 17 | 08 | 0 | 4 | 11 | 64 |
| | zk2905g5- | 53.6 | 46.8 | 0.0 | 0.0 | 0.0 | 0.0 | 0.0 | | | | 0.0 | 0.0 | 100. |
| Py4 | 2-3 | 77 | 04 | 35 | 52 | 82 | 06 | 1 | 0 | 0 | 0 | 53 | 02 | 72 |
| | zk2905g5- | 53.7 | 46.5 | 0.0 | 0.0 | | | 0.0 | 0.0 | 0.0 | 0.0 | 0.0 | | 100. |
| Py4 | 2-4 | 14 | 69 | 51 | 28 | 0 | 0 | 06 | 28 | 29 | 75 | 38 | 0 | 54 |
| | zk2905g5- | 53.7 | 46.4 | 0.0 | 0.0 | | | 0.0 | 0.0 | | 0.0 | 0.0 | | 100. |
| Py4 | 2-5 | 48 | 72 | 29 | 11 | 0 | 0 | 06 | 34 | 0 | 13 | 24 | 0 | 34 |
| | zk2905g5- | 53.7 | 46.3 | 0.0 | 0.0 | 0.0 | | | 0.0 | 0.1 | 0.0 | 0.0 | | 100. |
| Py4 | 2-6 | 5 | 85 | 38 | 28 | 73 | 0 | 0 | 07 | 09 | 08 | 17 | 0 | 42 |
| | zk2905g5- | 53.7 | 46.7 | 0.0 | | 0.0 | | | | 0.0 | | 0.0 | | 100. |
| Py4 | 2-7 | 84 | 36 | 41 | 0 | 03 | 0 | 0 | 0 | 33 | 0 | 77 | 0 | 67 |
| | zk2905g5- | 53.8 | 46.2 | 0.0 | 0.0 | | 0.0 | | | | 0.0 | 0.0 | | 100. |
| Py4 | 2-8 | 12 | 57 | 61 | 04 | 0 | 33 | 0 | 0 | 0 | 23 | 5 | 0 | 24 |
| | zk2905g5- | 53.8 | 46.8 | 0.0 | | | 0.0 | 0.0 | | | 0.0 | 0.0 | 0.0 | 100. |
| Py4 | 2-9 | 46 | 1 | 83 | 0 | 0 | 15 | 06 | 0 | 0 | 77 | 38 | 28 | 9 |
| | zk2905g5- | 53.4 | 46.1 | 0.0 | | 0.0 | | | | 0.1 | 0.0 | 0.0 | | 99.9 |
| Py4 | 2-10 | 46 | 5 | 61 | 0 | 4 | 0 | 0 | 0 | 42 | 74 | 6 | 0 | 73 |
| | zk2905g5- | 53.3 | 46.5 | 0.0 | 0.0 | | | 0.0 | | 0.0 | 0.0 | 0.0 | | 100. |
| Py4 | 2-11 | 46 | 53 | 57 | 37 | 0 | 0 | 39 | 0 | 67 | 43 | 14 | 0 | 16 |
| | zk2905g5- | 53.9 | 46.4 | 0.0 | 0.0 | | 0.0 | 0.0 | 0.0 | 0.0 | | 0.0 | 0.0 | 100. |
| Py4 | 2-12 | 05 | 26 | 32 | 48 | 0 | 09 | 53 | 12 | 3 | 0 | 22 | 06 | 54 |
| | zk2905g5- | 52.7 | 46.2 | 0.1 | 0.1 | 0.0 | 0.0 | | | 0.0 | | 0.0 | | 99.5 |
| Py4 | 2-13 | 64 | 74 | 34 | 69 | 95 | 21 | 0 | 0 | 4 | 0 | 59 | 0 | 56 |
| | zk2905g5- | 53.1 | 46.4 | 0.0 | | 0.0 | | | | 0.1 | 0.0 | 0.0 | | 99.8 |
| Py4 | 2-14 | 56 | 88 | 61 | 0 | 4 | 0 | 0 | 0 | 02 | 38 | 05 | 0 | 9 |

A total of 31 LA-ICP-MS trace element spot analyses were analyzed on pyrite from the Sanhetun Te-Au deposit (Table 2), including 10 spots on Py1, 10 spots on Py2, 6 spots on Py3 and 5 spots on Py4. The results reveal distinct trace element abundance in all stages of pyrite (Figure 8). Py1 displays the lowest concentration of detected trace elements except for Co and Ni, trace elements concentrations of Py1 are often at or below the detection limits. Py2 preserves slightly high As contents (59.24~1784.14 ppm) compared to Py1 (0~12.85 ppm), Py3 (0~6.01 ppm, except for one outlier) and Py4 (3.33~7.44 ppm). In addition to As, Py2 also shows the relatively higher concentration of elements such as Mo (163.94~625.39 ppm), Sb (4.65~53.07 ppm) and Mn (6.60~152.54 ppm). The main ore-stage Py3 has the highest Au (0.36~440.79 ppm), Ag (1.93~1758.18 ppm), Te (17.60~2801.51 ppm), Bi (0.61~196.02 ppm) and Pb (15.79~8651.72 ppm) contents. The Co content of Py3 deserve comment, they have very low Co content varying from 0.07 to 0.43 ppm except for one outlier. Compared to Py3, the post ore-stage Py4 shows the relatively lower concentration of elements including Te, Bi, Au and Ag.

 doi:10.20944/preprints202404.1971.v1



**Table 2.** LA-ICP-MS analyses of pyrite grains from the different stages in the Sanhetun Te-Au deposit (all values in ppm).

| Stage | Sample No. | Ti | Mn | Co | Ni | Cu | Zn | Ge | As | Se | Mo | Ag | Cd | Sb | Te | Au | Tl | Bi | Pb |
|---|---|---|---|---|---|---|---|---|---|---|---|---|---|---|---|---|---|---|---|
| Py1 | zk2904g7-1 | 1.35 | 0.00 | 34.42 | 24.56 | 0.00 | 0.28 | 4.86 | 0.00 | 0.00 | 0.16 | 0.00 | 0.19 | 0.02 | 0.22 | 0.01 | 0.01 | 0.01 | 0.02 |
| Py1 | zk2904g7-2 | 6.17 | 0.85 | 380.43 | 176.43 | 0.99 | 0.60 | 4.33 | 0.00 | 2.26 | 0.08 | 0.61 | 0.08 | 0.08 | 8.81 | 0.08 | 0.00 | 0.23 | 1.11 |
| Py1 | zk2904g7-3 | 5.59 | 0.11 | 26.51 | 31.80 | 7.12 | 0.18 | 4.79 | 4.97 | 0.00 | 0.04 | 5.08 | 0.06 | 0.85 | 21.36 | 2.11 | 0.05 | 2.53 | 18.90 |
| Py1 | zk2904g7-4 | 1.55 | 0.00 | 0.21 | 0.00 | 0.02 | 0.46 | 4.34 | 2.09 | 1.24 | 0.09 | 0.06 | 0.00 | 0.05 | 0.02 | 0.01 | 0.00 | 0.00 | 1.59 |
| Py1 | zk2904g7-5 | 2.63 | 0.00 | 8.16 | 4.21 | 1.21 | 0.71 | 4.64 | 0.52 | 2.08 | 0.05 | 0.01 | 0.00 | 0.00 | 4.63 | 0.02 | 0.02 | 0.06 | 0.19 |
| Py1 | zk2904g7-6 | 2.14 | 0.10 | 61.71 | 61.14 | 5.16 | 0.76 | 4.87 | 2.98 | 0.67 | 0.09 | 3.22 | 0.00 | 0.13 | 9.99 | 1.15 | 0.00 | 1.04 | 8.18 |
| Py1 | zk1001g2-1 | 0.93 | 0.00 | 102.41 | 16.64 | 0.74 | 0.62 | 5.16 | 12.85 | 2.02 | 0.04 | 1.20 | 0.01 | 0.08 | 4.06 | 0.15 | 0.01 | 1.36 | 2.17 |
| Py1 | zk1001g2-3 | 4.15 | 0.05 | 11.09 | 8.67 | 1.46 | 0.77 | 4.73 | 0.81 | 3.34 | 0.07 | 0.06 | 0.00 | 0.00 | 0.65 | 25.49 | 0.02 | 0.04 | 0.14 |
| Py1 | zk1001g2-4 | 1.21 | 0.00 | 53.04 | 24.08 | 0.78 | 0.14 | 4.23 | 2.44 | 0.69 | 0.08 | 0.79 | 0.00 | 0.00 | 2.08 | 0.29 | 0.00 | 0.16 | 1.38 |
| Py2 | zk2905g5-1-1 | 56.59 | 40.39 | 14.31 | 11.95 | 36.67 | 3.54 | 4.97 | 1784.14 | 2.73 | 163.94 | 20.18 | 0.38 | 14.85 | 117.89 | 8.59 | 0.28 | 61.29 | 215.34 |
| Py2 | zk2905g5-1-2 | 17.05 | 152.54 | 22.61 | 28.74 | 111.99 | 6.12 | 4.41 | 276.23 | 3.63 | 436.09 | 22.97 | 3.33 | 26.11 | 81.84 | 5.60 | 2.15 | 76.29 | 262.73 |
| Py2 | zk2905g5-1-3 | 18.30 | 40.62 | 20.29 | 23.37 | 74.76 | 4.60 | 4.55 | 350.11 | 1.96 | 282.92 | 18.59 | 0.96 | 11.83 | 73.66 | 5.65 | 0.55 | 60.60 | 217.15 |
| Py2 | zk2905g5-1-4 | 87.94 | 11.32 | 9.40 | 13.68 | 64.72 | 3.64 | 4.59 | 535.52 | 4.02 | 572.19 | 10.94 | 0.26 | 9.81 | 51.69 | 4.21 | 0.43 | 40.09 | 115.95 |
| Py2 | zk2905g5-1-5 | 4.66 | 7.87 | 3.55 | 6.65 | 59.57 | 3.45 | 4.33 | 59.24 | 0.84 | 625.39 | 4.87 | 0.66 | 4.65 | 11.43 | 2.03 | 0.67 | 10.15 | 40.36 |
| Py2 | zk2905g5-1-6 | 20.84 | 10.13 | 15.20 | 20.55 | 93.19 | 5.18 | 4.45 | 173.18 | 0.00 | 243.14 | 12.24 | 1.94 | 10.60 | 50.42 | 3.70 | 0.88 | 48.08 | 151.22 |
| Py2 | zk2905g5-1-7 | 60.30 | 6.60 | 15.08 | 15.86 | 57.98 | 3.84 | 4.93 | 372.96 | 0.31 | 436.00 | 9.84 | 1.34 | 16.28 | 35.50 | 3.16 | 0.81 | 40.76 | 163.58 |
| Py2 | zk2905g5-1-8 | 691.12 | 10.16 | 22.02 | 40.89 | 64.56 | 2.92 | 5.00 | 1194.13 | 1.04 | 359.57 | 5.60 | 1.00 | 53.07 | 26.45 | 3.12 | 2.06 | 10.98 | 369.50 |
| Py2 | zk2905g5-1-9 | 222.14 | 10.32 | 54.32 | 38.51 | 98.48 | 2.83 | 4.56 | 731.53 | 2.24 | 231.95 | 30.27 | 1.60 | 36.48 | 142.43 | 7.57 | 3.29 | 128.55 | 335.56 |
| Py2 | zk2905g5-1-10 | 102.91 | 16.09 | 15.77 | 18.57 | 62.97 | 5.81 | 5.17 | 213.34 | 1.06 | 286.36 | 21.23 | 2.66 | 19.07 | 75.39 | 4.73 | 1.99 | 81.51 | 142.46 |
| Py3 | zk1001g2-2 | 5.88 | 0.25 | 46.61 | 7.35 | 25.46 | 1.07 | 5.72 | 5.92 | 0.19 | 0.01 | 282.66 | 0.02 | 0.32 | 284.80 | 47.07 | 0.03 | 28.66 | 43.02 |
| Py3 | zk2905g3-1 | 1.58 | 0.00 | 0.20 | 18.43 | 414.41 | 0.56 | 4.13 | 3.15 | 0.85 | 0.07 | 1253.20 | 4.83 | 0.44 | 2021.51 | 250.14 | 0.03 | 104.29 | 8651.72 |
| Py3 | zk2905g3-2 | 1.50 | 0.21 | 0.36 | 87.78 | 44.87 | 0.44 | 4.60 | 6.01 | 4.21 | 0.06 | 542.55 | 2.44 | 0.98 | 716.70 | 99.76 | 0.05 | 80.14 | 4418.70 |
| Py3 | zk2905g3-3 | 1.51 | 0.00 | 0.41 | 83.01 | 62.20 | 0.54 | 4.66 | 3.78 | 0.75 | 0.18 | 1758.18 | 0.06 | 0.29 | 2801.51 | 440.79 | 0.00 | 26.64 | 209.25 |
| Py3 | zk2905g3-4 | 1.65 | 0.00 | 0.07 | 31.93 | 20.25 | 0.22 | 4.56 | 3.22 | 2.13 | 0.00 | 9.47 | 0.00 | 0.33 | 36.91 | 1.51 | 0.00 | 0.61 | 33.03 |
| Py3 | zk2905g3-5 | 1.06 | 0.23 | 0.43 | 21.37 | 7.54 | 0.49 | 4.89 | 0.00 | 1.77 | 0.07 | 1.93 | 0.49 | 0.20 | 17.60 | 0.36 | 0.01 | 0.92 | 15.79 |
| Py3 | zk2905g3-6 | 1.14 | 0.95 | 0.28 | 57.51 | 66.36 | 0.72 | 4.77 | 4752.33 | 0.77 | 0.08 | 598.01 | 0.36 | 18.00 | 1342.73 | 150.31 | 0.08 | 196.02 | 368.74 |
| Py4 | zk2905g5-1 | 2.25 | 0.00 | 3.67 | 3.36 | 9.63 | 0.43 | 4.17 | 5.99 | 2.00 | 0.02 | 1.16 | 0.02 | 0.00 | 17.07 | 0.60 | 0.00 | 19.27 | 21.63 |
| Py4 | zk2905g5-2 | 1.15 | 0.18 | 8.44 | 3.80 | 22.39 | 0.52 | 4.09 | 7.44 | 4.39 | 0.06 | 87.08 | 0.06 | 0.06 | 166.87 | 10.62 | 0.02 | 139.45 | 36.26 |
| Py4 | zk2905g5-3 | 1.94 | 0.14 | 12.39 | 5.11 | 13.79 | 0.45 | 5.09 | 5.61 | 3.87 | 0.00 | 3.78 | 0.11 | 0.12 | 35.95 | 1.14 | 0.00 | 40.94 | 40.93 |
| Py4 | zk2905g5-4 | 1.88 | 0.28 | 5.26 | 2.25 | 5.98 | 0.63 | 4.97 | 4.59 | 2.92 | 0.04 | 1.40 | 0.00 | 0.00 | 15.23 | 0.31 | 0.01 | 13.41 | 20.18 |
| Py4 | zk2905g5-5 | 2.00 | 0.07 | 21.68 | 4.83 | 6.69 | 0.68 | 4.75 | 3.33 | 2.25 | 0.02 | 1.29 | 0.00 | 0.10 | 19.05 | 0.24 | 0.00 | 10.73 | 13.66 |

 doi:10.20944/preprints202404.1971.v1



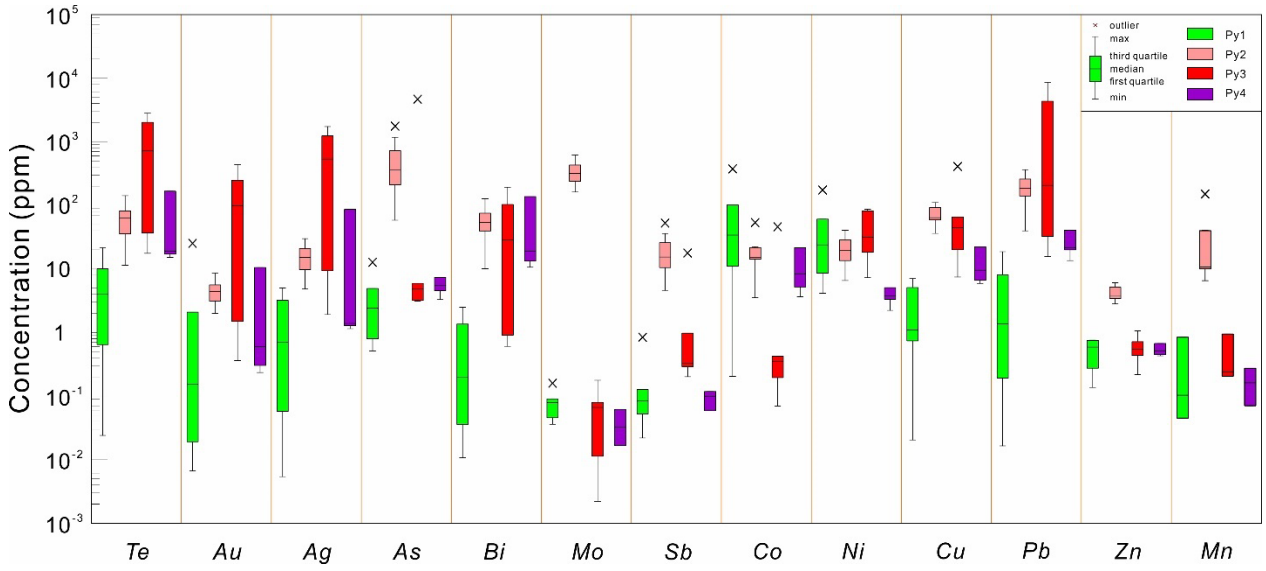


**Figure 8.** Box and whisker diagrams of trace element concentrations in pyrite from different stages.

*4.3. In Situ Sulfur Isotopic Composition*

A total of 35 spots were analyzed in situ for sulfur isotopic compositions by fs La-MC-ICP-MS. The S isotopic compositions of Sanhetun pyrites are presented in Table 3 and illustrated in Figure 9. The $\delta^{34}S$ values show a wide range of variation from −5.69 to +14.43‰ for the pyrite from Sanhetun Te-Au deposit with up to 20.12‰ difference, indicating that sulfur isotopic composition of ore forming fluids is heterogeneous. Py1 has slightly negative $\delta^{34}S$ values ranging from −1.20~−0.57‰ (mean=-0.8, n=7). Py2 are characterized by the most variable positive $\delta^{34}S$ values ranging from 4.67 to 14.43‰ (mean=8.23, n=10). Py3 display a $\delta^{34}S$ values ranging from −5.69~0.19‰ (mean=-2.89, n=10). Py4 has a narrow range of $\delta^{34}S$ values from 2.66 to 3.86‰ (mean=3.41, n=8).

**Table 3.** Sulfur isotopic compositions of pyrite from the Sanhetun Te-Au deposit.

| Stage | Sample no. | $\delta^{34}S_{V\text{-}CDT}$ (‰) |
|---|---|---|
| Py1 | ZK2904g7-1-1 | -0.85 |
| Py1 | ZK2904g7-1-2 | -0.66 |
| Py1 | ZK2904g7-1-3 | -1.20 |
| Py1 | ZK2904g7-1-4 | -0.65 |
| Py1 | ZK2904g7-1-5 | -0.57 |
| Py1 | ZK2904g7-1-6 | -0.69 |
| Py1 | ZK2904g7-1-7 | -0.95 |
| Py2 | ZK2905g5-1-1 | 14.43 |
| Py2 | ZK2905g5-1-2 | 11.09 |
| Py2 | ZK2905g5-1-3 | 5.33 |
| Py2 | ZK2905g5-1-4 | 6.59 |
| Py2 | ZK2905g5-1-5 | 6.88 |
| Py2 | ZK2905g5-1-6 | 11.03 |
| Py2 | ZK2905g5-1-7 | 6.78 |
| Py2 | ZK2905g5-1-8 | 4.75 |
| Py2 | ZK2905g5-1-9 | 4.67 |
| Py2 | ZK2905g5-1-10 | 10.78 |
| Py3 | ZK2905g3-1 | -0.74 |
| Py3 | ZK2905g3-2 | -5.69 |
| Py3 | ZK2905g3-3 | -4.38 |
| Py3 | ZK2905g3-4 | -5.44 |
| Py3 | ZK2905g3-5 | -5.16 |

 doi:10.20944/preprints202404.1971.v1



| | | |
|---|---|---|
| Py3 | ZK2905g3-6 | -4.69 |
| Py3 | ZK2905g3-7 | -0.89 |
| Py3 | ZK2905g3-8 | -1.09 |
| Py3 | ZK2905g3-9 | 0.19 |
| Py3 | ZK2905g3-10 | -1.03 |
| Py4 | ZK1001g2-1-1 | 2.90 |
| Py4 | ZK1001g2-1-2 | 2.66 |
| Py4 | ZK1001g2-1-3 | 3.05 |
| Py4 | ZK2905g5-1 | 3.62 |
| Py4 | ZK2905g5-2 | 3.65 |
| Py4 | ZK2905g5-3 | 3.86 |
| Py4 | ZK2905g5-4 | 3.76 |
| Py4 | ZK2905g5-5 | 3.78 |

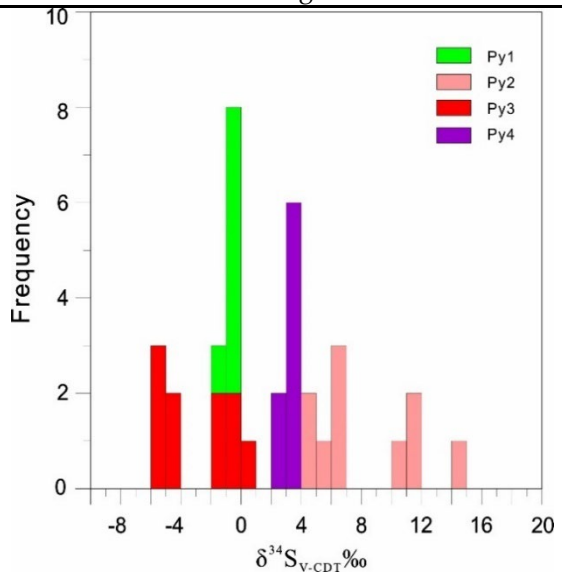


**Figure 9.** Sulfur isotopic compositions of pyrite from different stages.

*4.4. Calcite U-Pb Age*

The results of LA-ICP-MS U-Pb analyses for calcite are listed in Table 4. A total of 17 LA-ICP-MS spot analyses of calcite from the Stage II yielded U and Pb contents of 0.43 to 8.73 ppm (mean = 5.03 ppm) and 0.82 to 39.36 ppm (mean = 14.62 ppm), respectively. On the Tera-Wasserburg diagram (Figure 10), the data yield a lower intercept age of 135 ± 22 Ma (MSWD = 0.64).

**Table 4.** LA-ICP-MS data for stage II calcite in the Sanhetun Te-Au deposit.

| Sample no. | Contents (ppm) | | | $^{238}U/^{206}Pb$ | | $^{207}Pb/^{206}Pb$ | |
|---|---|---|---|---|---|---|---|
| | U | Th | Pb | Ratio | 2σ | Ratio | 2σ |
| Zk2905g5-1 - 1 | 0.43 | 0.43 | 0.82 | 1.7658 | 0.1382 | 0.8021 | 0.0164 |
| Zk2905g5-1 - 2 | 2.18 | 0.52 | 2.13 | 2.9919 | 0.2550 | 0.7909 | 0.0121 |
| Zk2905g5-1 - 7 | 3.31 | 0.49 | 4.29 | 2.7224 | 0.1216 | 0.7936 | 0.0149 |
| Zk2905g5-1 - 8 | 4.48 | 0.60 | 5.60 | 2.4515 | 0.1727 | 0.7934 | 0.0106 |
| Zk2905g5-1 - 9 | 3.39 | 0.68 | 4.55 | 2.3182 | 0.1292 | 0.8022 | 0.0106 |
| Zk2905g5-3 - 1 | 6.04 | 1.42 | 16.58 | 0.9071 | 0.0712 | 0.8225 | 0.0071 |
| Zk2905g5-3 - 2 | 7.99 | 1.62 | 30.65 | 0.8609 | 0.0267 | 0.8266 | 0.0081 |
| Zk2905g5-3 - 3 | 6.26 | 1.72 | 30.37 | 0.6643 | 0.0296 | 0.8278 | 0.0077 |
| Zk2905g5-3 - 4 | 5.15 | 3.84 | 36.04 | 0.5622 | 0.0089 | 0.8297 | 0.0062 |
| Zk2905g5-3 - 5 | 8.16 | 7.34 | 39.36 | 0.7759 | 0.0359 | 0.8308 | 0.0076 |
| Zk2905g5-3 - 6 | 4.05 | 2.64 | 28.05 | 0.5598 | 0.0086 | 0.8322 | 0.0079 |
| Zk2905g5-4 - 1 | 4.67 | 2.14 | 7.06 | 1.9161 | 0.1121 | 0.8045 | 0.0119 |

 doi:10.20944/preprints202404.1971.v1



| | | | | | | | |
|---|---|---|---|---|---|---|---|
| Zk2905g5-4 - 2 | 5.43 | 1.63 | 8.95 | 1.9336 | 0.0887 | 0.8104 | 0.0096 |
| Zk2905g5-4 - 3 | 3.68 | 1.19 | 4.73 | 2.7463 | 0.1258 | 0.8090 | 0.0168 |
| Zk2905g5-4 - 4 | 8.73 | 2.85 | 18.42 | 1.7070 | 0.0517 | 0.8164 | 0.0099 |
| Zk2905g5-4 - 5 | 5.25 | 1.36 | 8.83 | 2.1261 | 0.0735 | 0.7978 | 0.0107 |
| Zk2905g5-4 - 6 | 5.58 | 2.27 | 8.25 | 2.1815 | 0.1156 | 0.8036 | 0.0104 |
| Zk2905g5-4 - 7 | 5.71 | 2.03 | 8.45 | 1.9677 | 0.1210 | 0.8083 | 0.0080 |

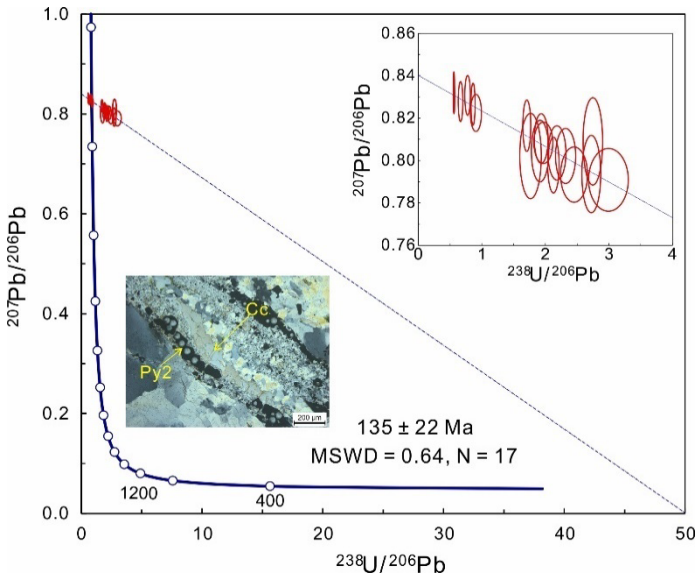


**Figure 10.** The U-Pb Tera-Wasserburg diagram for calcite in Stage II from the Sanhetun Te-Au deposit.

## 5. Discussion

### *5.1. Trace Element Distribution in Pyrite*

Previous studies have highlighted that pyrite can incorporate different types of trace elements in different forms. These elements commonly occur as solid solution dissolved in the pyrite structure, visible mineral inclusions or invisible nanoparticles dispersed within the pyrite[22–25]. Here, we mainly concentrated on the distribution and occurrence of As, Au and Te in different stages of pyrite from the Sanhetun Te-Au deposit. Arsenic is one of the most common trace elements in pyrite, which can serve as either $As^{2+/3+}$ replacing $Fe^{2+}$ or as $As^{-}$ replacing $S^{-}$ during isomorphic substitution or as amorphous $As^{0}$ nanoparticles[26–30]. EMPA data suggest that pyrite within the Sanhetun Te-Au deposit is As-free (<0.1 wt%). LA-ICP-MS data also shows that all types of pyrite are deficient in As, even though Py2 has slightly high As content. Previous studies show that As and Au have coupled geochemistry in pyrite from multiple types of gold deposits[31,32]. However, the As-Au binary diagram shows that there is no clear correlation between the concentrations of Au and As (Figure 11a). This diagram also shows that the data points of Py1, Py2 and Py4 fall into below the Au saturation line indicating that the dominant form of gold is found as solid solution, data points of Py3 however fall in the area above the line suggesting that Au occur as Au nanoparticles or Au-bearing submicroscopic mineral inclusions. Keith et al. (2018) proposed that the incorporation of Te and Au in pyrite is likely governed by a similar process and further hypothesized that the Au saturation line may also be applicable to Te [28]. In the As-Te binary diagram (Figure 11b), the data points of different stages of pyrite mostly plot above the Au saturation line indicating that Te most likely presents as the Te-bearing mineral inclusions in the Sanhetun Te-Au deposit. This interpretation is supported by LA-ICP-MS time-resolved depth profile (Figure 12). Py1 and Py2 commonly have the discontinuous or smooth profiles for Te and Au, implying that the Te and Au are mainly distributed as the solid solution within the Py1 and Py2 (Figure 12a,b). With regard to the Py3 and Py4, the LA-ICP-MS profiles for Au, Bi and Te are generally synchronously ragged, indicating

 doi:10.20944/preprints202404.1971.v1



that the presence of Te-Bi-Au inclusions (Figure 12c,d). Ciobanu et al. (2012) reported the occurrence of nanoparticles of Au-telluride in As-free pyrite by direct observation using transmission electron microscopy (TEM). These nanoparticles are able to contribute to a large proportion of Au budget in As-free pyrite [23].

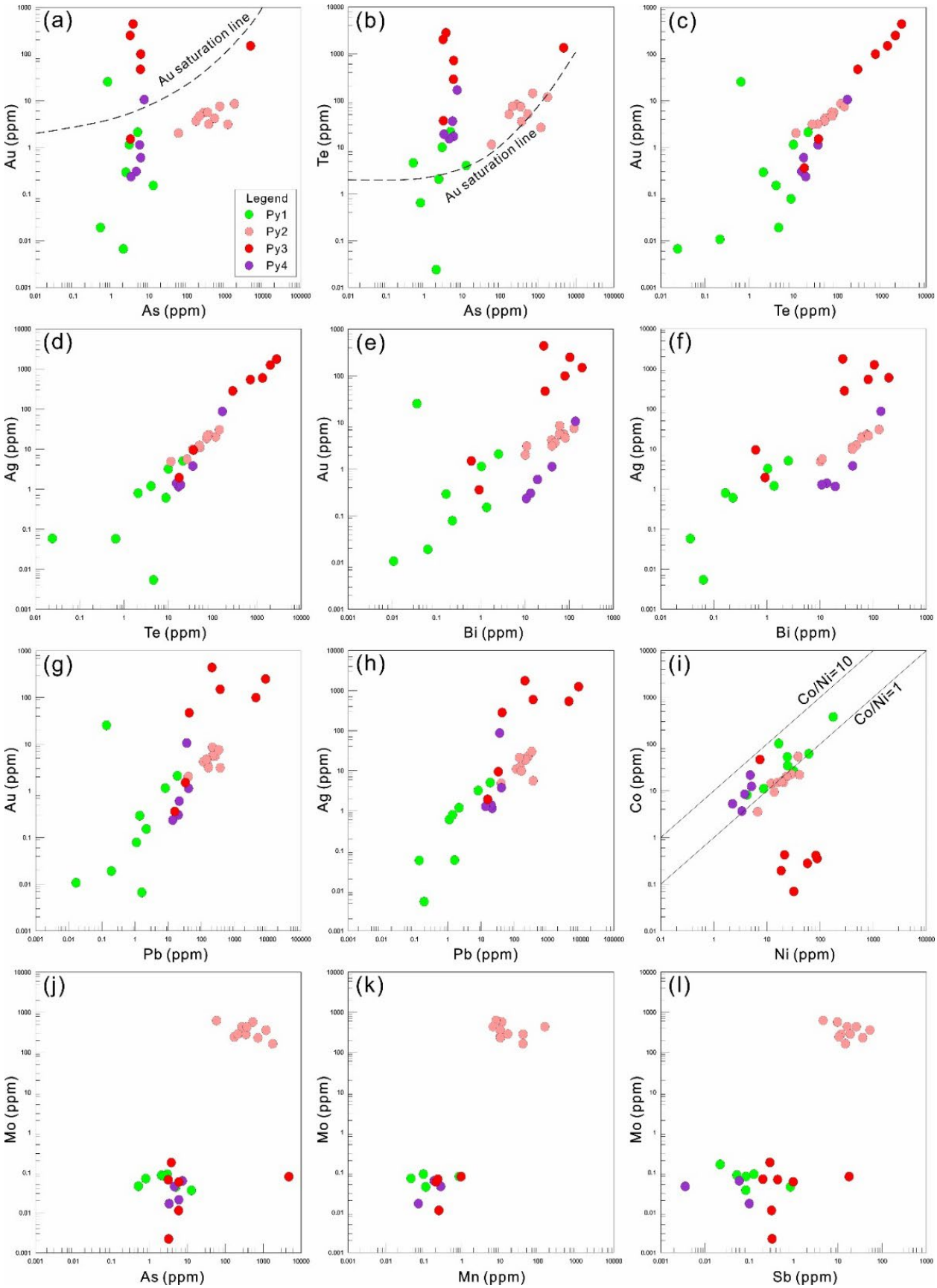

 doi:10.20944/preprints202404.1971.v1



**Figure 11.** Bivariate plots of trace elements in different types of pyrite from Sanhetun Te-Au deposit. Au saturation line after [32].

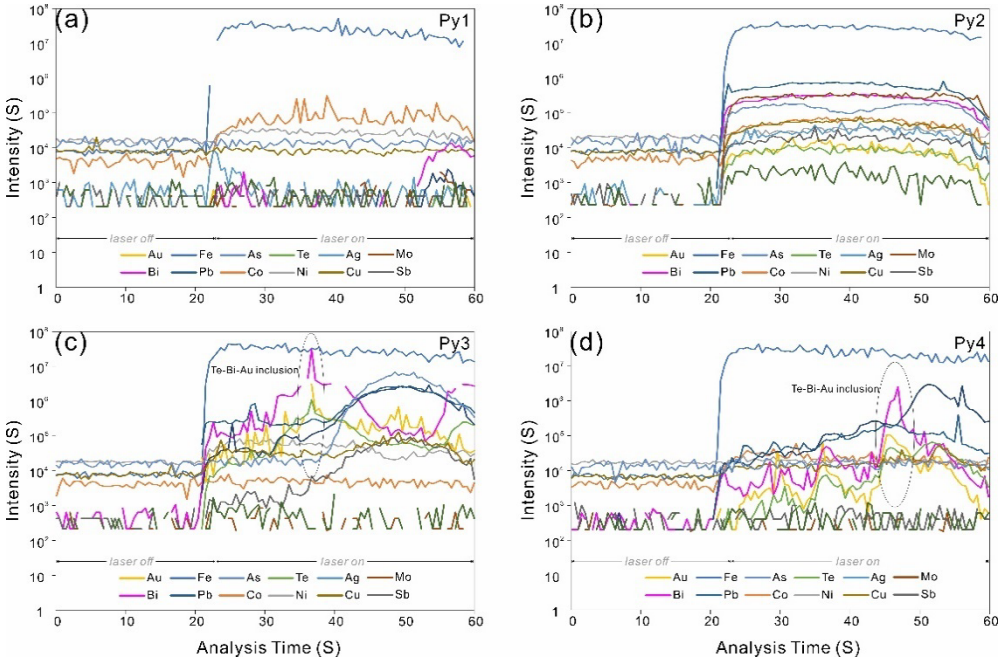


**Figure 12.** Representative LA-ICP-MS time-resolved depth profiles for different types of pyrite from Sanhetun Te-Au deposit.

*5.2. Genesis of Pyrites*

The trace element and S isotopes of pyrite can provide critical information to understand the source and evolution of the ore-forming fluids[33–35]. Based on the mineral assemblage, crosscutting relationships, trace element and S isotopes of pyrite, four types of pyrite have been recognized from the Sanhetun Te-Au deposit.

The pre-ore stage Py1 is significantly deficient in Au, Ag, As, Te and other trace elements except for Co and Ni and has narrow range of $\delta^{34}S$ values from −1.20~−0.57‰. The relatively uniform $\delta^{34}S$ values of Py1 indicate that the ore-forming fluids were probably derived from a homogeneous sulfur source. The $\delta^{34}S$ values closing to 0 suggest that magmatic sulfur could generate the $\delta^{34}S$ range for Py1. There is little Au and Te to precipitation in this stage.

The Py2 exhibits distinguishable features of trace element and $\delta^{34}S$ composition in comparison with other generations of pyrite. They are featured by the relatively high concentrations of As, Mo, Sb, Zn and Mn (Figure 11j–l) with a wide range of variations of remarkably positive $\delta^{34}S$ values from 4.67 to 14.43‰. The characteristics of Py2 indicate that the remarkably positive $\delta^{34}S$ was contributed by the wall-rock mylonite. In addition, previous study shows the mylonite has the relatively high concentrations of Te (0.17 ppm) and Au (0.02 ppm) [36], indicating that the mylonite might supply part of Te and Au to the formation of Sanhetun Te-Au deposit.

The main ore stage Py3 contains the highest Au, Ag, Te and Bi concentrations with the negative $\delta^{34}S$ values from -5.69 to 0.19‰. The negative $\delta^{34}S$ values could be ascribe as several reasons, including biogenic or sedimentary sulfur origin and isotope fractionation driven by high oxygen fugacity and boiling of magmatic-derived fluids[37,38]. Among these reasons, sulfur isotope fractionation under the high oxygen fugacity is the most possible mechanism causing the negative $\delta^{34}S$ values of pyrite. Tellurium is widely recognized for its high solubility in ore-forming fluids under high oxygen fugacity conditions, however, under more reduced conditions, its solubility experiences a significant decrease[28,39,40]. This is in line with the highest concentrations of Te in the Py3. This conclusion is also supported by the occurrence of rutile within the Py3. In addition, previous studies have suggested that the ratio of Bi/Te (+S, Se) in phases belonging to the tetradymite group can serve as an indicator of the redox conditions of ore-forming fluids. Phases with a Bi/Te (+S, Se) ratio greater

 doi:10.20944/preprints202404.1971.v1



than 1 are typically associated with reduced conditions, whereas those with a Bi/Te (+S, Se) ratio less than 1 indicate oxidized conditions[41,42]. The Sanhetun Te-Au deposit contains abundant tetradymite ($Bi_2Te_2S$) which have Bi/Te (+S, Se) <1 ratio indicating that the ore-forming fluids were in oxidizing conditions. It is worth noting that the Py3 has very low Co contents and Co/Ni ratios. The Co and Ni contents in pyrite can reflect the temperature and origin of pyrite. Cobalt prefers to be incorporated in pyrite at high temperatures, while Ni prefers to incorporate in pyrite at low temperatures[43,44]. Hence, the low Co contents may be caused by a sudden cooling process in the ore-forming fluids.

The Py4 contains relatively low Te and Au with the slightly positive $\delta^{34}S$ values from 2.66 to 3.86‰. Such $\delta^{34}S$ values are similar to the usual estimate of $\delta^{34}S$ values for magmatic sulfur [45], implying that magmatic sulfur could generate the $\delta^{34}S$ range for Py4. The Co/Ni ratios of Py4 are generally > 1 further supporting that ore-forming fluids are magmatic fluids. Petrographic observation shows that the majority of telluride coexists with Py4. However, Py4 are commonly lack of Au indicating that the majority of Au deposit in the Py3. The precipitation of a large number of sulfide consumed large amounts of sulfur leading to the increasing of $fTe_2/fS_2$. The elevated $fTe_2/fS_2$ ratios give rise to the deposition of telluride in Py4, especially native tellurium which reflects the high Te fugacity of the ore-forming fluids.

### *5.3. Enrichment Mechanism of Au*

The mechanism of Au enrichment is crucial to understanding the genesis of gold deposits. Several mechanisms have been proposed by previous studies, including rapid decrease of Au solubility [46], coupled dissolution-reprecipitation (CDR) [47], electrochemical accumulation of Au[48,49], fault-valve processes [50], and low melting chalcophile elements (LMCE) melt collector model[51–56]. The enrichment mechanism of Au in the Sanhetun is still unclear since it is a newly discovered gold deposit. In the Sanhetun deposit, a number of Te-Bi minerals were recognized, particularly tetradymite which has the close relationship with native gold. Both Te and Bi are LMCE, the role they played in scavenging Au and other precious metals has been widely researched[47,53,54,57–60]. Especially Bi, the liquid bismuth collector model was proved to be a highly efficient enrichment mechanism of Au based on theoretical calculations and experiments verification[52,53]. In comparation with Bi, there are relatively few convincing studies proving tellurium act as the Au scavenger. Recently, Jian et al. (2021, 2024) proposed that Te-rich melts can continue to scavenge gold from Au-undersaturated ore-forming fluids leading to the growth of melts and giving rise to the enrichment of Au[54,55]. In the Sanhetun deposit, native gold is the main Au-bearing minerals, which generally intergrown with tetradymite (Figure 4f,g). The binary plots of trace elements of pyrites (Figure 11c,e) show a remarkably positive correlation between Te, Bi and Au, indicating that they have strong geochemical affinity. In other words, tellurium and Bi may play a critical role in governing Au enrichment. The native gold and tetradymite mineral assemblage show element combinations of Au-Te-Bi-S. Because of the low melting temperatures of Te-Bi phases (down to 266°C [61]), they could occur as melt droplets in the ore-forming fluids in the Sanhetun. The Te-Bi-S melts will efficiently scavenge Au from ore-forming fluids, even if the fluids are highly undersaturated[52,53]. This scavenging process results in the forming of nanometer to micrometer scale Au-Te-Bi-S melts. The cooling of micrometer scale melts leads to the formation of native gold and tetradymite assemblage, which is proved by the petrographic observation. The nanometer scale ones will be trapped within pyrite, which is confirmed by the time-resolved profiles showing the simultaneous spiky signal of Au, Te and Bi in Py3 and Py4 (Figure 12c,d). In summary, we suggest that Au enrichment of the Sanhetun Te-Au deposit is closely related to the existence of Te-Bi-S melts in the Au-undersaturated ore-forming fluids.

### *5.4. Timing of Te-Au Mineralization*

The precise age of mineralization is critical to understand the ore genesis[62–64]. On account of the lack of suitable uranium(U)-rich minerals, it is difficult to constrain the accurate age of Te-Au mineralization in Sanhetun directly. Recently, with the advancement of in situ microanalysis

 doi:10.20944/preprints202404.1971.v1



technology, low U minerals, such as calcite, can be used for in situ U-Pb dating [65]. Calcite, as the common gangue mineral, generally coexists with Te-Au-bearing pyrite in the Sanhetun deposit. It could be an ideal potential dating minerals to reveal the timing of Te-Au mineralization. Petrographic observation shows that calcite commonly coexist with the Py2 and its age is able to represent the early stage of mineralization age at Sanhetun. In this study, we report the first calcite U-Pb age of 135 ± 22 Ma (n = 17, MSWD = 0.64), representing an early stage of Te-Au mineralization. These ages suggest that the Sanhetun Te-Au deposit occurred in the Early Cretaceous. In NE China, there are widespread Early Cretaceous volcanic rocks related to the subduction of Paleo-Pacific plate [66]. The sulfur isotope compositions in this study suggest that the ore-forming materials were mainly derived from deep seated magma source with a minor contribution from mylonite. Previous study concluded that Te tends to enrich in the oceanic Fe-Mn crust leading it to be a potential reservoir for Te resource in the ocean[67,68]. Hence, the Te-rich magma might be derived from the partial melting of mantal which is metasomatized by the Te-rich fluids originated from oceanic sediments. Based on the information above, we conclude that the formation of Sanhetun Te-Au deposit may be related to the subduction of the Paleo-Pacific plate in the Early Cretaceous.

## 6. Conclusions

(1) Five species of telluride were recognized in the Sanhetun Te-Au deposit, including native Te, tetradymite, tsumoite, hessite and petzite. Tetradymite commonly have close relationship with native gold.
(2) Tellurium occurs as solid solution hosted in the lattice of Py1 and Py2 and Te-Bi-Au submicroscopic inclusions concealing in Py3 and Py4. Gold is mainly present as visible gold and subordinately as invisible gold which occurs as Te-Bi-Au submicroscopic inclusions.
(3) Au enrichment of the Sanhetun Te-Au deposit might be attributed to the existence of Te-Bi-S melts, which can act as an important gold scavenger in the Au-undersaturated ore-forming fluids.
(4) LA-ICP-MS U-Pb dating of calcite from the ore stage revealed the Te-Au mineralization at Sanhetun occurred at 135 Ma during the Early Cretaceous. The S isotopes data suggest a deep source for the metals. Our geochronological and geochemical data suggest that the formation of Sanhetun Te-Au deposit might be related to the subduction of Paleo Pacific plate in Early Cretaceous.

**Author Contributions:** Investigation, M.Z., C.L. and H.G.; data curation, K.X. and G.Z.; writing—original draft preparation, M.Z.; writing—review and editing, J.S.; funding acquisition, J.L. and C.L; writing—review and editing, M.S. All authors have read and agreed to the published version of the manuscript.

**Funding:** This research was funded by Major Research Plan of National Natural Science Foundation of China (Grant No.92062219) and Northeast Geological S&T Innovation Center of China Geological Survey (Grant No. QCJJ2022-16).

**Data Availability Statement:** The data presented in this study are available.

**Acknowledgments:** We greatly thank anonymous reviewers and editors for the constructive comments that helped to improve this paper.

**Conflicts of Interest:** The authors declare no conflict of interest.

**References**

1. Gao, R.; Xue, C.; Lü, X.; Zhao, X.; Yang, Y.; Li, C. Genesis of the Zhengguang gold deposit in the Duobaoshan ore field, Heilongjiang Province, NE China: Constraints from geology, geochronology and S-Pb isotopic compositions. *Ore Geol. Rev.* **2017**, *84*, 202-217.
2. Liu, J.; Li, Y.; Zhou, Z.; OuYang, H. The Ordovician igneous rocks with high Sr/Y at the Tongshan porphyry copper deposit, satellite of the Duobaoshan deposit, and their metallogenic role. *Ore Geol. Rev.* **2017**, *86*, 600-614.
3. Suo, Q.; Shen, P.; Li, C.; Feng, H.; Chu, X. Mineral chemistry and apatite Sr isotope signatures record overprinting mineralization in the Duobaoshan porphyry Cu deposit, Heilongjiang Province, NE China. *Ore Geol. Rev.* **2023**, *162*, 105718.

4. Chen, J.; Wang, K.; Cai, W.; Geng, J.; Xue, H.; Wang, X. Fluid evolution and genesis of the Sankuanggou Fe -Cu skarn deposit, Duobaoshan ore field, Northeast China: Evidence from fluid inclusions and H-O-S-Pb isotopes. *J. Geochem. Explor.* **2023**, *252*, 107251.
5. Yang, H.; Ma, W.L.; Cai, W.Y.; Wang, K.Y.; Sun, F.Y.; Wang, J.H.; Zhou, H.Y.; Kou, B.Y. Metallogenic epoch and tectonic setting of the Xiaoduobaoshan Fe-Cu deposit in Heilongjiang Province, China: Evidence from petrogeochemistry, zircon U-Pb geochronology and Hf isotopic compositions (in Chinese with English abstract). *Acta Petrol. Sin.* **2020**, *36*, 856-870.
6. Zhai, D.G.; Williams-Jones, A.E.; Liu, J.J.; Tombros, S.F.; Cook, N.J. Mineralogical, Fluid Inclusion, and Multiple Isotope (H-O-S-Pb) Constraints on the Genesis of the Sandaowanzi Epithermal Au-Ag-Te Deposit, NE China. *Econ. Geol.* **2018**, *113*, 1359-1382.
7. Zhang, M.; Shen, J.; Santosh, M.; Li, C.; Liu, H.; Yu, H.; Kamoto, M.; Du, B.; Liu, J. Tellurium and Gold enrichment aided by melts and pyrite crystallization kinetics: Insights from the Yongxin gold deposit, Northeast China. *Ore Geol. Rev.* **2023**, *156*, 105370.
8. Li, C.L.; Li, L.; Yuan, M.W.; Alam, M.; Li, S.R.; Santosh, M.; Deng, C.Z.; Liu, H.; Xu, G.Z. Study on pyrite thermoelectricity, ore-forming fluids and H-O-Rb-Sr isotopes of the Yongxin gold deposit, Central Asian Orogenic Belt: Implications for ore genesis and exploration. *Ore Geol. Rev.* **2020**, *121*, 103568.
9. Yuan, M.W.; Li, S.R.; Li, C.L.; Santosh, M.; Alam, M.; Zeng, Y.J. Geochemical and isotopic composition of auriferous pyrite from the Yongxin gold deposit, Central Asian Orogenic Belt: Implication for ore genesis. *Ore Geol. Rev.* **2018**, *93*, 255-267.
10. Li, C.; Deng, C.; Li, S.; Yuan, M.; Alam, M.; Liu, B.; Zhao, Z.; Li, W.; Yang, Y. Geochronology and genesis of the newly discovered Mengdehe orogenic-type Au deposit in the Xing'an-Mongolia orogenic Belt, NE China. *Ore Geol. Rev.* **2021**, *133*, 104083.
11. Gao, S.; Xu, H.; Zang, Y.Q.; Wang, T. Mineralogy, ore-forming fluids and geochronology of the Shangmachang and Beidagou gold deposits, Heilongjiang province, NE China. *J. Geochem. Explor.* **2018**, *188*, 137-155.
12. McNulty, B.A.; Jowitt, S.M. Byproduct critical metal supply and demand and implications for the energy transition: A case study of tellurium supply and CdTe PV demand. *Renew. Sust. Energ. Rev.* **2022**, *168*.
13. Zweibel, K. The impact of Tellurium supply on Cadmium Telluride photovoltaics. *Science* **2010**, *328*, 699-701.
14. Fornari, C.I.; Bentmann, H.; Morelhão, S.L.; Peixoto, T.R.F.; Rappl, P.H.O.; Tcakaev, A.; Zabolotnyy, V.; Kamp, M.; Lee, T.; Min, C.; Kagerer, P.; Vidal, R.C.; Isaeva, A.; Ruck, M.; Hinkov, V.; Reinert, F.; Abramof, E. Incorporation of Europium in $Bi_2Te_3$ topological insulator epitaxial films. *The Journal of Physical Chemistry C* **2020**, *124*, 16048-16057.
15. Steven, B.; William, M.; Jinxue, W.; Michael, J.; Farzin, A. Advances in HgCdTe APDs and LADAR receivers. *Proc.Spie* **2010**, *7660*.
16. Gu, H.J.; Li, B.W.; Li, C.L.; Yang, W.P.; Yang, Y.J.; Shi, H.L.; Zhang, M.M. The Discovery and Significance of Tellurideinthe Sanhetun Gold Deposit inthe Northeastern Great Xing'an Range (in Chinese with English abstract). *Mineral. Petrol.* **2023**, *43*, 94-104.
17. Liu, B.S.; Kou, L.L.; Zhang, C.P.; Li, C.L.; Luo, J.; Han, R.P.; Li, B.W. Research on the relationship between mineralization and zircon LA-ICP-MS U-Pb dating of the mylonite from the Sanhetun gold deposit in Nenjiang region, Heilongjiang Province (in Chinese with English abstract). *Acta Geologica Sinica* **2022**, *96*, 954-970.
18. Zhou, J.; Wilde, S.A.; Zhao, G.; Han, J. Nature and assembly of microcontinental blocks within the Paleo-Asian Ocean. *Earth-Sci. Rev.* **2018**, *186*, 76-93.
19. Miao, L.C.; Fan, W.M.; Zhang, F.Q.; Liu, D.Y.; Jian, P.; Shi, G.H.; Tao, H.; Shi, Y.R. Zircon SHRIMP geochronology of the Xinkailing-Keluo complex in the northwestern Lesser Xing'an Range, and its geological implications. *Chinese Science Bulletin* **2003**, *48*, 2315-2323.
20. Li, B.W.; Gu, H.J.; Li, C.L.; Liu, B.S.; Yang, X.P. Geological Characteristics and Prospecting Potential of Sanhetun Gold Deposit in Heilongjiang Province (in Chinese with English Abstract). *Gold Science and Technology* **2022**, *30*, 508-517.
21. Wang, F.Y.; Ge, C.; Ning, S.Y.; Nie, L.Q.; Zhong, G.X.; White, N.C. A new approach to LA-ICP-MS mapping and application in geology (in Chinese with English abstract). *Acta Petrologica Sinica* **2017**, *33*, 3422-3436.
22. Deditius, A.P.; Utsunomiya, S.; Reich, M.; Kesler, S.E.; Ewing, R.C.; Hough, R.; Walshe, J. Trace metal nanoparticles in pyrite. *Ore Geol. Rev.* **2011**, *42*, 32-46.
23. Ciobanu, C.L.; Cook, N.J.; Utsunomiya, S.; Kogagwa, M.; Green, L.; Gilbert, S.; Wade, B. Gold-telluride nanoparticles revealed in arsenic-free pyrite. *Am. Miner.* **2012**, *97*, 1515-1518.
24. Gregory, D.D.; Large, R.R.; Halpin, J.A.; Baturina, E.L.; Lyons, T.W.; Wu, S.; Danyushevsky, L.; Sack, P.J.; Chappaz, A.; Maslennikov, V.V.; Bull, S.W. Trace Element Content of Sedimentary Pyrite in Black Shales. *Econ. Geol.* **2015**, *110*, 1389-1410.

25. Zhang, J.; Deng, J.; Chen, H.; Yang, L.; Cooke, D.; Danyushevsky, L.; Gong, Q. LA-ICP-MS trace element analysis of pyrite from the Chang'an gold deposit, Sanjiang region, China: Implication for ore-forming process. *Gondwana Res.* **2014**, *26*, 557-575.
26. Deditius, A.P.; Utsunomiya, S.; Ewing, R.C.; Kesler, S.E. Nanoscale "liquid" inclusions of As-Fe-S in arsenian pyrite. *Am. Miner.* **2009**, *94*, 391-394.
27. Fleet, M.E.; Mumin, A.H. Gold-bearing arsenian pyrite and marcasite and arsenopyrite from Carlin Trend gold deposits and laboratory synthesis. *Am. Miner.* **1997**, *82*, 182-193.
28. Keith, M.; Smith, D.J.; Jenkin, G.R.T.; Holwell, D.A.; Dye, M.D. A review of Te and Se systematics in hydrothermal pyrite from precious metal deposits; insights into ore-forming processes. *Ore Geol. Rev.* **2018**, *96*, 269-282.
29. Deditius, A.P.; Utsunomiya, S.; Renock, D.; Ewing, R.C.; Ramana, C.V.; Becker, U.; Kesler, S.E. A proposed new type of arsenian pyrite: Composition, nanostructure and geological significance. *Geochim. Cosmochim. Acta* **2008**, *72*, 2919-2933.
30. Qian, G.; Brugger, J.; Testemale, D.; Skinner, W.; Pring, A. Formation of As(II)-pyrite during experimental replacement of magnetite under hydrothermal conditions. *Geochim. Cosmochim. Acta* **2013**, *100*, 1-10.
31. Deditius, A.P.; Reich, M.; Kesler, S.E.; Utsunomiya, S.; Chryssoulis, S.L.; Walshe, J.; Ewing, R.C. The coupled geochemistry of Au and As in pyrite from hydrothermal ore deposits. *Geochim. Cosmochim. Acta* **2014**, *140*, 644-670.
32. Reich, M.; Kesler, S.E.; Utsunomiya, S.; Palenik, C.S.; Chryssoulis, S.L.; Ewing, R.C. Solubility of gold in arsenian pyrite. *Geochim. Cosmochim. Acta* **2005**, *69*, 2781-2796.
33. Barker, S.L.L.; Hickey, K.A.; Cline, J.S.; Dipple, G.M.; Kilburn, M.R.; Vaughan, J.R.; Longo, A.A. Uncloaking invisible gold: use of nanoSIMS to evaluate gold, trace elements, and sulfur isotopes in pyrite from Carlin-type gold deposits. *Econ. Geol.* **2009**, *104*, 897-904.
34. Tanner, D.; Henley, R.W.; Mavrogenes, J.A.; Holden, P. Sulfur isotope and trace element systematics of zoned pyrite crystals from the El Indio Au–Cu–Ag deposit, Chile. *Contrib. Mineral. Petrol.* **2016**, *171*, 33.
35. Du, B.; Shen, J.; Santosh, M.; Liu, H.; Liu, J.; Wang, Y.; Xu, K. Textural, compositional and isotopic characteristics of pyrite from the Zaozigou gold deposit in West Qinling, China: Implications for gold metallogeny. *Ore Geol. Rev.* **2021**, *130*, 103917.
36. Li, C. Characteristics of Structural Superimposed Halo and Deep Prospecting Prediction of Yongxin Gold Deposit, Duobaoshan Area, Heilongjiang Province (in Chinese with English abstract). *Geoscience* **2023**, *37*, 674-689.
37. Ohmoto, H. Systematics of Sulfur and Carbon Isotopes in Hydrothermal Ore Deposits. *Econ. Geol.* **1972**, *67*, 551-578.
38. Chaussidon, M.; Lorand, J. Sulphur isotope composition of orogenic spinel lherzolite massifs from Ariege (North-Eastern Pyrenees, France): An ion microprobe study. *Geochim. Cosmochim. Acta* **1990**, *54*, 2835-2846.
39. Cooke, D.R.; McPhail, D.C. Epithermal Au-Ag-Te Mineralization, Acupan, Baguio District, Philippines: Numerical Simulations of Mineral Deposition. *Econ. Geol.* **2001**, *96*, 109-131.
40. Grundler, P.V.; Brugger, J.; Etschmann, B.E.; Helm, L.; Liu, W.; Spry, P.G.; Tian, Y.; Testemale, D.; Pring, A. Speciation of aqueous tellurium(IV) in hydrothermal solutions and vapors, and the role of oxidized tellurium species in Te transport and gold deposition. *Geochim. Cosmochim. Acta* **2013**, *120*, 298-325.
41. Ciobanu, C.L.; Birch, W.D.; Cook, N.J.; Pring, A.; Grundler, P.V. Petrogenetic significance of Au–Bi–Te–S associations: The example of Maldon, Central Victorian gold province, Australia. *Lithos* **2010**, *116*, 1-17.
42. Cook, N.J.; Ciobanu, C.L.; Wagner, T.; Stanley, C.J. MINERALS OF THE SYSTEM Bi–Te–Se–S RELATED TO THE TETRADYMITE ARCHETYPE: REVIEW OF CLASSIFICATION AND COMPOSITIONAL VARIATION. *The Canadian Mineralogist* **2007**, *45*, 665-708.
43. Zhen, S.; Wang, D.; Yu, X.; Wang, Q.; Li, Y.; Zha, Z.; Wang, J. Trace Elements and Sulfur Isotopes of Sulfides in the Zhangquanzhuang Gold Deposit, Hebei Province, China: implications for physicochemical conditions and mineral deposition mechanisms. *Minerals* **2020**, *10*.
44. Maslennikov, V.V.; Maslennikova, S.P.; Large, R.R.; Danyushevsky, L.V. Study of Trace Element Zonation in Vent Chimneys from the Silurian Yaman-Kasy Volcanic-Hosted Massive Sulfide Deposit (Southern Urals, Russia) Using Laser Ablation-Inductively Coupled Plasma Mass Spectrometry (LA-ICPMS). *Econ. Geol.* **2009**, *104*, 1111-1141.
45. Rye, R.O. A review of the stable-isotope geochemistry of sulfate minerals in selected igneous environments and related hydrothermal systems. *Chem. Geol.* **2005**, *215*, 5-36.
46. Williams-Jones, A.E.; Bowell, R.J.; Migdisov, A.A. Gold in Solution. *Elements* **2009**, *5*, 281-287.
47. Cook, N.J.; Ciobanu, C.L.; Mao, J.W. Textural control on gold distribution in As-free pyrite from the Dongping, Huangtuliang and Hougou gold deposits, North China Craton (Hebei Province, China). *Chem. Geol.* **2009**, *264*, 101-121.
48. Möller, P.; Kersten, G. Electrochemical accumulation of visible gold on pyrite and arsenopyrite surfaces. *Miner. Depos.* **1994**, *29*, 404-413.

 doi:10.20944/preprints202404.1971.v1




49. Laird, J.S.; Halfpenny, A.; Ryan, C.G.; Liu, W. Evidence supporting micro-galvanic coupling in sulphides leads to gold deposition. *Contrib. Mineral. Petrol.* **2021**, *176*, 1-19.
50. Peterson, E.C.; Mavrogenes, J.A. Linking high-grade gold mineralization to earthquake-induced fault-valve processes in the Porgera gold deposit, Papua New Guinea. *Geology* **2014**, *42*, 383-386.
51. Douglas, N.; Mavrogenes, J.; Hack, A.; England, R. The liquid bismuth collector model: An alternative gold deposition mechanism, in Skilbeck, C.G., and Hubble, T.C.T., eds., Understanding planet Earth; searching for a sustainable future; on the starting blocks of the third millennium: Australian Geological Convention, 15th, Sydney, Abstracts: Sydney, Geological Society of Australia, 135 p. **2000**.
52. Tooth, B.; Brugger, J.; Ciobanu, C.; Liu, W. Modeling of gold scavenging by bismuth melts coexisting with hydrothermal fluids: An experimental study. *Geology* **2008**, *36*, 815-818.
53. Tooth, B.; Ciobanu, C.L.; Green, L.; O Neill, B.; Brugger, J. Bi-melt formation and gold scavenging from hydrothermal fluids: An experimental study. *Geochim. Cosmochim. Acta* **2011**, *75*, 5423-5443.
54. Jian, W.; Mao, J.W.; Lehmann, B.; Cook, N.J.; Xie, G.Q.; Liu, P.; Duan, C.; Alles, J.; Niu, Z.J. Au-Ag-Te-rich melt inclusions in hydrothermal gold-quartz veins, Xiaoqinling Lode Gold District, central China. *Econ. Geol.* **2021**, *116*, 1239-1248.
55. Jian, W.; Mao, J.; Lehmann, B.; Cook, N.J.; Li, J.; Song, S.; Zhu, L. Hyper-enrichment of gold via quartz fracturing and growth of polymetallic melt droplets. *Geology* **2024**.
56. Frost, B.R.; Mavrogenes, J.A.; Tomkins, A.G. Partial melting of sulfide ore deposits during medium- and high-grade metamorphism. *The Canadian Mineralogist* **2002**, *40*, 1-18.
57. Cockerton, A.B.D.; Tomkins, A.G. Insights into the Liquid Bismuth Collector Model Through Analysis of the Bi-Au Stormont Skarn Prospect, Northwest Tasmania. *Econ. Geol.* **2012**, *107*, 667-682.
58. Oberthur, T.; Weiser, T.W. Gold-bismuth-telluride-sulphide assemblages at the Viceroy Mine, Harare-Bindura-Shamva greenstone belt, Zimbabwe. *Mineral. Mag.* **2008**, *72*, 953-970.
59. Pals, D.W.; Spry, P.G. Telluride mineralogy of the low-sulfidation epithermal Emperor gold deposit, Vatukoula, Fiji. *Mineral. Petrol.* **2003**, *79*, 285-307.
60. Bi, S.J.; Li, J.W.; Zhou, M.F.; Li, Z.K. Gold distribution in As-deficient pyrite and telluride mineralogy of the Yangzhaiyu gold deposit, Xiaoqinling district, southern North China craton. *Miner. Depos.* **2011**, *46*, 925-941.
61. Okamoto, K.; Tanner, L.E. Bi-Te (bismuth-tellurium). In: Massalski, T.B., Ohamoto, K. (Eds.), Binary Alloy Phase Diagrams. Ohio, ASM International, Materials Park, Ohio. **1990**, 800-801.
62. Deng, J.; Qiu, K.F.; Wang, Q.F.; Goldfarb, R.; Yang, L.Q.; Zi, J.W.; Geng, J.Z.; Ma, Y. In situ dating of hydrothermal monazite and implications for the geodynamic controls on ore formation in the Jiaodong gold province, eastern China. *Econ. Geol.* **2020**, *115*, 671-685.
63. Zhai, D.G.; Liu, J.J.; Zhang, A.L.; Sun, Y.Q. U-Pb, Re-Os, and $^{40}$Ar-$^{39}$Ar geochronology of porphyry Sn ± Cu ± Mo and polymetallic (Ag-Pb-Zn-Cu) vein mineralization at Bianjiadayuan, Inner Mongolia, Northeast China: Implications for discrete mineralization events. *Econ. Geol.* **2017**, *112*, 2041-2059.
64. Xu, J.; Liu, X.; Lai, J.; He, H.; Song, X.; Zhai, D.; Li, B.; Wang, Y.; Shi, J.; Zhou, X. In Situ U-Pb Geochronology of Calcite from the World's Largest Antimony Deposit at Xikuangshan, Southern China. *Minerals* **2022**, *12*.
65. Zhang, L.L.; Zhu, D.C.; Yang, Y.H.; Wang, Q.; Xie, J.C.; Zhao, Z.D. U-Pb Geochronology of Carbonate by Laser Ablation MC-ICP-MS: Method Improvements and Geological Applications. *Atom. Spectrosc.* **2021**, *42*, 335-348.
66. Wu, F.; Lin, J.; Wilde, S.A.; Zhang, X.; Yang, J. Nature and significance of the Early Cretaceous giant igneous event in eastern China. *Earth Planet. Sci. Lett.* **2005**, *233*, 103-119.
67. Hein, J.R.; Koschinsky, A.; Halliday, A.N. Global occurrence of tellurium-rich ferromanganese crusts and a model for the enrichment of tellurium. *Geochim. Cosmochim. Acta* **2003**, *67*, 1117-1127.
68. Hein, J.R.; Koschinsky, A.; Kuhn, T. Deep-ocean polymetallic nodules as a resource for critical materials. *Nat. Rev. Earth Environ.* **2020**, *1*, 158-169.